



HAL
open science

NiCo and NiCo Decorated with Ru Nanoparticles for Magnetically Induced Hydroprocessing of Lignin Models

Jaime Mazarío, Irene Mustieles Marin, Gabriel Mencia, Christian Wittee Lopes, Víctor Varela-Izquierdo, Giovanni Agostini, Pier-Francesco Fazzini, Nicolas Ratel-Ramond, Bruno Chaudret

► To cite this version:

Jaime Mazarío, Irene Mustieles Marin, Gabriel Mencia, Christian Wittee Lopes, Víctor Varela-Izquierdo, et al.. NiCo and NiCo Decorated with Ru Nanoparticles for Magnetically Induced Hydroprocessing of Lignin Models. ACS Applied Nano Materials, 2024, 7 (8), pp.9412-9427. 10.1021/ac-sanm.4c00895 . hal-04642070

HAL Id: hal-04642070

<https://hal.science/hal-04642070>

Submitted on 9 Jul 2024

HAL is a multi-disciplinary open access archive for the deposit and dissemination of scientific research documents, whether they are published or not. The documents may come from teaching and research institutions in France or abroad, or from public or private research centers.

L'archive ouverte pluridisciplinaire **HAL**, est destinée au dépôt et à la diffusion de documents scientifiques de niveau recherche, publiés ou non, émanant des établissements d'enseignement et de recherche français ou étrangers, des laboratoires publics ou privés.

Magnetically Induced Hydroprocessing of Lignin Models using Organometallic NiCo and NiCo@Ru Nanoparticles

J. Mazarío,^{1#} I. Mustieles Marin,^{1#} G. Mencia,¹ C.W. Lopes,² V. Varela-Izquierdo,¹ G. Agostini,³ P.F. Fazzini,⁴ N. Ratel-Ramond,¹ B. Chaudret,^{1*}

¹ *Université de Toulouse, UMR 5215 INSA, CNRS, UPS, Laboratoire de Physique et Chimie des Nano-Objets, 135 avenue de Rangueil F-31077 Toulouse cedex 4, France*

² *Department of Chemistry, Federal University of Paraná (UFPR), Curitiba, 81531-990, Brazil*

³ *CELLS-ALBA Synchrotron Radiation Facility, 08290 Cerdanyola del Vallés, Barcelona, Spain*

⁴ *CEMES-CNRS, Université de Toulouse, CNRS, 29 rue Jeanne Marvig, 31055 Toulouse, France*

Both authors contributed equally to this work

*chaudret@insa-toulouse.com

Abstract

A series of bimetallic Ni_{10-x}Co_x (x: 2, 3, 4, 5) nanoparticles has been prepared using the organometallic approach from Ni[PrNC(CH₃)N'Pr]₂ and Co[N(SiMe₃)₂]₂(thf) precursors. Structural characterization by High-Resolution Transmission Electron Microscopy (HR-TEM), X-ray absorption spectroscopy (XAS), and X-ray diffraction (XRD) revealed a bimetallic structure with an fcc Ni-rich core and ultra-small (≤ 2 nm) hcp Co nanoparticles decorating it. Magnetic and magnetic hyperthermia properties were measured through Vibrating Sample Magnetometry (VSM) and calorimetry, respectively. Moreover, the Ni₇Co₃ composition was shown to be a stable heterogeneous catalyst for diphenylether (DPE) hydrogenation under magnetic induction. Remarkably, the Ni₇Co₃ system before and after its decoration with a small amount of Ru (1 wt.%) was transposed to the low-pressure hydrogenation of lignin linkage models and lignin oil molecules. The results showed that the system had moderate activity in cleaving different ether C—O bonds and was effective in upgrading lignin oils through HDO, with a significant preference to produce cyclohexanols. This study represents a significant step towards applications of magnetic-induced catalysis in the field of biomass valorization.

INTRODUCTION

Encouraged by a genuine concern about climate change and the depletion of fossil feedstocks, the scientific community is striving to fulfil the growing demand for chemicals and fuels produced from sustainable raw materials. (1,2) These alternatives must also fit into the evolving energy market, which is relying more and more on intermittent renewable sources. (3-5)

Interestingly, *magnetically induced catalysis*, where the catalyst combines heating and catalytic function, has been proven to bring about specific advantages, including high energy efficiency, very high and localized heating, and rapid heating and cooling. These pluses make it perfect for accommodating

intermittent energy sources. (6-8) Moreover, we have recently shown that induction heating can raise temperatures in the vicinity of magnetic nanoparticles (MagNPs) way beyond the boiling point of the solvent. (9) In recent years, this phenomenon has enabled chemical transformations under H₂ pressure and bulk temperature conditions where, otherwise, the catalytic performance would be insufficient. (10-15)

On the other hand, as for sustainable raw materials, *Lignin* is crucial in the shift needed by the chemical industry due to its substantial contribution to lignocellulosic biomass. However, it is harder to turn into usable fuels and chemicals than cellulose and hemicellulose due to its higher degree of polymerization, and heterogeneous spectrum of chemical moieties. (16,17)

Lignin's aromatic network consists mainly of three units: p-coumaryl, coniferyl, and sinapyl alcohols; highly interconnected by C–O and C–C linkages including β-O-4, α-O-4, 4-O-5 and β–β, β-5, β-4, 5–5. (18) As a first valorization step, lignin oil or bio-oil can be obtained by depolymerizing lignin through reductive catalytic fractionation (RCF) of lignocellulosic material. Additionally, many different treatments on native or isolated lignin, such as pyrolysis, (19,20) solvolysis, (21) reductive depolymerization, (22,23) acid-base depolymerization (24) or oxidative alkaline depolymerization (25) have been used to yield lignin oils, determining product distribution. Lignin oil comprises a wide range of smaller aromatics where phenols usually prevail, but also acids, aldehydes, and ketones. Among the reductive depolymerization methods, catalytic hydrogenolysis is an atom-economical strategy for cleaving C–O bonds, works in a neutral medium, and prevents repolymerization. Nonetheless, the process usually requires harsh conditions (H₂ pressures much greater than 10 bar) and a significant amount of noble metal in the catalyst. (16,17)

Furthermore, most applications require lignin oil to undergo catalytic hydrodeoxygenation (HDO) to reduce its oxygen content. Then, the resultant upgraded products (phenolics, cyclohexanols, aromatic hydrocarbons, and cycloalkanes) can be components or precursors of fuels and chemicals. (26,27) Specifically, to upgrade lignin oil, metal sulfide and noble metal catalysts are used, but both have drawbacks. Metal sulfides require extra sulfur (H₂S or C₂S) to preserve activity, leading to pollution of the resulting oil, while noble metals are expensive. Therefore, designing affordable and efficient HDO catalysts is crucial for lignin oil upgrading. (27-29)

Remarkably, bimetallic nanoparticles are commonly used in lignin hydrogenolysis and upgrading research due to desirable synergies based on electronic or geometric effects between the two metals. (30-32) In this line, we previously used the organometallic approach to synthesize non-noble bimetallic nanoparticles (i.e., FeCo, (33,34) FeNi, (35)) with controlled size, composition, and magnetic properties. Herein, we focus on the nickel-cobalt system. While nickel is known to present a good ability for hydrogen dissociation, the addition of cobalt has been associated with enhanced hydrogen adsorption and a higher ability to weaken the C–O bond; which have been attributed to an electronic transfer between Co and Ni. (36,37) But, not only from a catalytic viewpoint but also from a magnetic perspective, the combination is appealing. In fact, Co is a “hard magnetic material” displaying very high

anisotropy and, therefore, no heating power at low field amplitudes, but high Curie temperature, while Ni is a “soft magnet”, with a lower anisotropy, requiring lower field amplitudes to release heat, but also with a lower Curie temperature. (38)

Accordingly, we transferred the organometallic synthesis protocol to the preparation of several NiCo MagNPs, starting from an unreported combination of metal precursors. The precursors chosen were $\text{Ni}[\text{PrNC}(\text{CH}_3)\text{N}'\text{Pr}]_2$ and $\text{Co}[\text{N}(\text{SiMe}_3)_2](\text{thf})$, exhibiting similar decomposition rates, thus assuring the presence of both metals in the final NPs. Samples with different Ni:Co ratios were prepared, aiming at finding the right balance between magnetic heating and catalytic properties. The nanoparticles (NPs) were fully characterized by HR-TEM/STEM, XAS, and XRD to disentangle their structure at the atomic level and by VSM and SAR to ascertain magnetic and hyperthermia properties. The efficiency of these NPs in magnetically induced lignin depolymerization via hydrogenolysis and hydrodeoxygenation was tested by using them in the hydrogenation of various lignin linkage models and bio-oil models, respectively. On the one hand, anisole, guaiacol, vanillin, cresol and eugenol, were used as typical model compounds to probe catalyst performance for lignin derivatives upgrading to arenes, cyclohexanes and cyclohexanols. On the other hand, lignin model compounds, including diphenyl ether (DPE), 4-phenoxyphenol, 4-benzyloxyphenol, and 2-phenoxy-1-phenylethanol, were used to evaluate the cleavage of the ether C–O bonds in 4-O-5, α -O-4, and β -O-4 linkages. Eventually, a small amount of Ru was added to NiCo NPs to enhance C–O cleavage and improve catalyst prospects for lignin depolymerization. Catalytic results make this catalytic system a promising beginning to accomplish lignin hydroprocessing under an alternating magnetic field and low H_2 pressures.

EXPERIMENTAL SECTION

All air-sensitive procedures were carried out either under an inert atmosphere of argon inside a glovebox or in a schlenk line. Diphenylether (>99 %), 2-phenoxy-1-phenylethanol (99%), 4-benzyloxyphenol (98%), 4-phenoxyphenol (99%), m-cresol (99%), vanillin (99%), eugenol (98%), guaiacol (99%), anisole (>99%), benzene (99.8%), cyclohexane (99%), ethylcyclohexane (99%), cyclohexanol (99%), ethylbenzene (99.8%), phenol (99.5%), benzylphenylether (98%), phenylethanol (98%), 1,4-cyclohexanediol (99%), toluene (99.7%), vanillin alcohol (99%), 2-methoxy-4-methylphenol (98%), 2-methoxycyclohexane (95%), 3-methylcyclohexanone (97%), cys-3-methylcyclohexanol (95%), 4-propylcyclohexanol (98%), propylbenzene (98%), propylcyclohexane (98%), 2-methoxy-4-propylphenol (99%), 4-propylphenol (98%), 1,4-cyclohexanediol (99%), 1-phenylethanol (98%), decane anhydrous ($\geq 99\%$) dodecane anhydrous ($\geq 99\%$) and dichloromethane (99.8%) were purchased from Sigma-Aldrich. 1-(4-hydroxy-3,5-dimethoxyphenyl)-2-(2-methoxyphenoxy)propane-1,3-diol (95%) was purchased from Biosynth. All these reactants were used without any additional purification and stored in a glove box under Ar atmosphere. THF (99%) and toluene (99%) for synthesis were purchased from VWR ProLabo and dried by passage through alumina and degassed with Ar before use.

Synthesis of Ni_{10-x}Co_x-NPs. NiCo NPs presenting different compositions were prepared using an organometallic approach in a 100 mL Fisher–Porter bottle (FP) under an inert argon atmosphere inside a glovebox. The synthesis employed metal precursors Ni[ⁱPrNC(CH₃)NⁱPr]₂ and Co[N(SiMe₃)₂]₂(thf) from *Nanomeps* and H₂(g). The stabilizing ligand was palmitic (PA) from Sigma-Aldrich (≥99%). All these reactants were used without any additional purification and stored in a glove box under Ar atmosphere. The solvent was mesitylene from VWR Prolabo (99%), dried by passage through alumina and degassed with Ar before use. In a general procedure, the Co complex was dissolved in 4 mL of mesitylene, followed by the addition of the Ni complex dissolved in another 6 mL of mesitylene. Regardless of the NP composition, the total metal concentration was maintained constant in the synthesis procedure (2.3 M). 1 equivalent of PA (593 mg) per metallic center was dissolved in 8 mL of mesitylene and added to the previous mixture under stirring. The Fisher Porter was then sealed, purged with Ar, evacuated and charged with 3 bars of H₂ (above atmospheric pressure) using a Schlenk line. An induction time of 40 min at room temperature after introducing the H₂ was also found necessary for a good definition of the NPs. Then, the FP was added to an oil bath at 120 °C and stirred vigorously (750 rpm) for 24 hours. After this time, it was transferred to a glovebox and cooled to room temperature with a magnet on the side to recover the magnetic NPs. The solution was decanted, and the NPs were then washed three times with 5 mL of toluene and dried under vacuum. Around 140 mg of a black magnetic solid are obtained, regardless of their composition.

Synthesis of Ni₇Co₃@Ru-NPs. For the decoration of the NiCo NPs with Ru, 80 mg of Ni₇Co₃-NPs and 18 mL of THF were added to a 100 mL FP inside the glovebox. Then, PA was added until a state where the NiCo NPs were dispersed under stirring (≈0.04 equivalents of PA; 10.4 mg). Afterwards, 0.04 equivalents (14.2 mg) of [Ru(cod)(cot)] (cod = 1,5-cyclooctadiene; cot = 1,3,5-cyclooctatriene) were dissolved in 2 mL of THF and added to the previous mixture. The FP was sealed, and the mixture was stirred (800 rpm) for 30 minutes at room temperature. After this time, the mixture was sonicated to enhance static NP dispersion, and 2 bars of H₂ (above atmospheric pressure) were added while sonicating after the evacuation of the Ar atmosphere. After charging, the mixture is kept for 2 minutes under sonication, where changes in the agglomeration state of the NPs can be seen. The mixture was then left for 2 h at room temperature under stirring (800 rpm). After this time, the NPs were isolated by magnetic decantation, washed 3 times with 5 mL of THF, and dried under vacuum. Around 80 mg of Ni₇Co₃@Ru are obtained.

Ni_{10-x}Co_x-NPs and Ni₇Co₃@Ru compositions. The metal and organic contents of the NPs were analyzed separately. The metal content was determined using ICP-MS (Pascher laboratory) after digestion in aqua regia at 80 °C for 12 h, whereas the organic content was determined using thermogravimetric analyses (TGA) in a TGA/DSC 1 STAR System equipped with an ultra-microbalance UMX5, a gas switch, and sensors DTA and DSC. The procedure to determine the metallic content involves oxidizing the sample under an air flow (50 mL·min⁻¹) up to 500 °C, followed by reduction under a mixed flow of 4% H₂ – 96% Ar (50 mL·min⁻¹) up to 700°C.

Transmission Electron Microscopy (TEM). The size and the morphology of the NPs were studied by Brightfield TEM (BF-TEM) imaging performed using a JEOL microscope (Model 1400) working at 120 kV. Additionally, deeper insight into the morphology and metal distribution in the nanoparticle was achieved by high-resolution (HR) BF-TEM and high-resolution Scanning Transmission Electron Microscopy (HR-STEM) analyses carried out with a Probe Corrected JEOL JEM-ARM200F microscope (cold FEG source), equipped with HAADF JEOL and BF JEOL detectors, working at 200 kV. STEM-EDX analysis was carried out with a High-Angle EDX SDD CENTURIO-X (129 eV resolution) detector attached to the JEOL JEM-ARM200F microscope. In all cases, TEM grids were prepared by deposition of one drop of a colloidal solution containing the NPs in toluene on a copper grid covered with amorphous carbon. HR micrograph analysis and fast Fourier transform (FFT) were done using the Gatan Digital Micrograph software (Gatan Inc.). The software ImageJ was used to obtain particle size distributions that were analyzed in terms of Gaussian statistics to get the mean size and standard deviation parameters.

X-Ray Absorption Spectroscopy. XAS experiments at the Co (7709 eV) and Ni (8333 eV) K-edges were performed at the NOTOS beamline of the ALBA Spanish synchrotron (Cerdanyola del Vallès, Spain). The white beam was monochromatized using a Si (111) water-cooled double crystal; harmonic rejection was performed using two Rh-coated silicon mirrors. Around 10 mg of NiCo-NPs were mixed with cellulose (ca. 100 mg) and pressed into disks in a sample holder covered with Kapton® tape. The spectra were collected in fluorescence mode using a 13-channel Silicon Drift Detector (SDD). Metallic Co and Ni foils were used as references for data alignment, which were located between the I1 and I2 ionization chambers. Several spectra were collected for each sample to ensure spectra reproducibility and a good signal-to-noise ratio. Data reduction and extraction of $\chi(k)$ were performed using the IFEFFIT package. (39) Only one Debye-Waller factor was adopted for Ni K-edge to decrease the number of variables in the fit. In the case of Co-K-edge, one Debye-Waller factor for each scattering path (Co-O and Co-Co) was necessary to obtain a coherent fit. More details on the EXAFS fits can be found in the table summarizing the obtained values (Table 1; *Results and Discussion*).

X-ray Diffraction (XRD). Routine XRD measurements for majority crystalline phase identification were carried out in reflection geometry on a PANalytical Empyrean diffractometer using Co-K α radiation ($\lambda=0.1789$ nm), operating at 35 kV and 45 mA. Data were collected over a 2θ range of $20\text{--}130^\circ$, with a step size of 0.08° and a time per step of 500 s for a total acquisition time of 45 min. To prevent oxidation, the powder samples were prepared and sealed with Kapton® polyimide films under an argon atmosphere.

In order to acquire higher quality data, some XRD measurements were performed in transmission geometry on a PANalytical Empyrean diffractometer using Mo-K α radiation ($\lambda=0.7107$ nm), operating at 60 kV and 40 mA and equipped with an incident focusing mirror combined with a GalipiX detector. Data were collected over a 2θ range of $3\text{--}140^\circ$, with a step size of 0.03° and a time for step of 8000 s, for a total acquisition time of 23 h. Glass capillaries of 500 μm diameter were filled with the powder samples under an argon atmosphere, and further sealed with a flame to prevent from specimen oxidation. Phase

identification was completed by a Rietveld analysis using GSASII software (40) performed on the Ni₆Co₄ system to ascertain the structures and fractions of the Ni and Co phases within the specimen.

Vibrating Sample Magnetometry (VSM). Magnetic measurements were carried out using a physical property measurement system (PPMS, Quantum Design) in the vibrating sample magnetometer configuration (VSM). The sample was prepared inside the glovebox as a dry powder (ca. 10 mg) enclosed in a Teflon capsule. The hysteresis loops were measured for magnetization vs. magnetic field at 300 K and 5 K, using an external field of up to ± 3 T.

Specific Absorption Rate (SAR). The SAR values were estimated using calorimetry experiments with a 93 kHz fixed frequency coil, following an optimized protocol described in our previous works. (35,41) In a typical experiment, a glass sample tube was charged under an inert atmosphere with the Mag-NPs (ca. 12 mg) and the organic solvent (0.5 mL, typically dry mesitylene). The Mag-NPs were dispersed in the solvent by sonication for a few seconds after sealing the tube with a Teflon-lined screw cap. During the calorimetric experiments, the sample tube was placed in the center of a magnetic coil filled with 1.8 mL of deionized water. Two optic fiber temperature probes are submerged in water, one near the socket's bottom and the other near its center. Then, the increase in temperature after applying an alternating magnetic field for 50 seconds is measured at different field amplitudes. The sample was exposed to field amplitudes varying between 0 and 47 mT. After applying a pre-calculated correction factor that accounts for the heat losses to the surroundings, it is possible to construct a curve of SAR ($W \cdot g^{-1}$) against field amplitude (mT).

Magnetically induced catalytic tests with model substrates. In a typical experiment, 1 mmol of substrate was dissolved in 5 mL of solvent together with 0.7 mmol of dodecane (internal standard) and around 8 mg of NPs (metal-substrate ratio always kept at 1:10 mol). Solvents were selected based on catalyst compatibility, boiling point, substrate solubility, and nanoparticle dispersion measured by dynamic light scattering (DLS) in a Nanotrack device, employing analogous concentrations to those used in the catalytic tests (4 mg in 2.5 mL), and sonicating 30 s before analysis (see SI, *Section 3.1*). The catalytic tests were carried out with a 100 mL FP reactor placed at the center of a 13.1 kW coil (*Fives Celes*, 5 cm height and 4 cm width) working at 300 kHz with an amplitude adjustable from 0-64 mT, and under 3 bars of H₂. Magnetic field amplitude optimization was conducted for those substrates showing low reaction rates (i.e., vanillin, m-cresol, and monobenzene; see SI, *Section 3.2*). After the reaction, the NPs were separated using a magnet and allowed to cool down to room temperature. The pressure of the flask was then released. The reaction mixture was filtered through celite, and approximately 10 drops of the filtered solution were diluted in 1.6 mL of dichloromethane (DCM) for analytical purposes. Only the final points were analyzed, and no sampling was done during the reaction. These mixtures were analyzed with a gas chromatograph (GC PerkinElmer 580), equipped with a BP-5 column (30 m length), and using H₂ as carrier gas. The GC is coupled to a Clarus SQ8T mass spectrometer for product identification and an FID detector for quantification. In all cases, the FID detector was used through the internal standard methodology (with dodecane) to calculate the different components in the reaction

mixture. Figs. S14-S22 show typical chromatograms obtained in this study. Based on these analyses, substrates conversions (X), yields on carbon basis (Y_i^{CB}) to the different products “i”, and carbon balances (CB) have been calculated by comparing peak areas of reagents, products, and internal standard, and applying the following formulas:

$$X_{\text{substrate}}(\text{mol.}\%) = \frac{n_{\text{substrate}}^f}{n_{\text{substrate}}^0} \cdot 100$$

$$Y_i^{CB}(\text{mol.}\%) = \frac{n_i \cdot x_i C_{\text{atoms}}}{n_{\text{substrate}}^0 \cdot y_{\text{substrate}} C_{\text{atoms}}} \cdot 100$$

$$CB(\text{mol}\%) = \frac{\sum n_{\text{product}_i}^f \cdot x_i C_{\text{atoms}}}{n_{\text{substrate}}^0 \cdot y_{\text{substrate}} C_{\text{atoms}}} \cdot 100$$

Being x_i the number of carbon atoms in the product i coming from the substrate reaction and $y_{\text{substrate}}$ the number of carbon atoms in the starting substrate.

Catalytic tests with DPE and conventional heating. The experimental procedure and starting reagent amounts were the same as those in the analogous experiment using magnetic-induced catalysis. However, instead of using the magnetic coil, the 100 mL FP bottle was placed in a preheated oil bath at 180 °C. The temperature of 180 °C was selected to achieve a bulk solution temperature above that registered by the IR camera in magnetically induced catalysis, as well as to ensure some reflux at 3 bars of H_2 pressure. Sample preparation and analyses followed the same procedures described above for magnetic-induced catalytic tests.

Magnetically induced catalytic tests with a lignin-oil model mixture. Another set of tests was conducted using a substrate mixture to imitate lignin oil. The mixture was composed of 0.20 mmol of *m*-cresol, 0.20 mmol of vanillin, 0.20 mmol of eugenol, 0.20 mmol of guaiacol and 0.20 mmol of anisole. Additionally, 0.25 mmol of decane was added as internal standard. This mixture was dissolved with 3 mL of decane and 2 mL of THF. To evaluate the $Ni_7Co_3@Ru$ upgrading performance under magnetic induction, reactions were carried out at different times, with a 100 mL FP reactor placed at the center of the 300 kHz coil mentioned above, working with a field amplitude of 65 mT, and under 3 bars of H_2 . Sample preparation and analysis followed the same protocols as previously described for individual substrates.

Magnetically induced catalytic tests with an advanced lignin model. The catalytic activity of the $Ni_7Co_3@Ru$ -NPs in lignin depolymerization was further investigated by using 1-(4-hydroxy-3,5-dimethoxyphenyl)-2-(2-methoxyphenoxy)propane-1,3-diol, a phenolic β -O-4 type C model compound. (42) In that sense, several reactions were conducted at different times with 0.1 mmol of this molecule, 1.5 mg of $Ni_7Co_3@Ru$ and 1.0 mL of deuterated THF (THF- d_8). In this case, a 10 mL FP reactor was placed at the center of the 300 kHz coil, working with a field amplitude of 65 mT and under 3 bars of H_2 (above atmospheric pressure). Product identification was accomplished by using a combination of GC-MS and

NMR analyses on a 500 MHz Bruker Avance spectrometer. Diffusion-Ordered Spectroscopy (DOSY) showed a major product with a similar diffusion constant as the substrate (9.89×10^{-10} and 9.33×10^{-10} $\text{m}^2 \cdot \text{s}^{-1}$, respectively), which means a minor transformation. This product was found to be 4-(3-hydroxy-2-(2-methoxyphenoxy)propyl)-2,6-dimethoxyphenol (dhLIGM). Its characteristic multiplets, resulting from the HDO reaction on the benzylic carbon, are observed as doublets of doublets ($^2J_{\text{H-H}}=13.9$ Hz, $^3J_{\text{H-H}}=6.3$ Hz) at 2.9 ppm with a pronounced roof effect. The proposed structure of this molecule agrees with the m/z (334.8) found by GC-MS. Moreover, 2D-Totally Correlated Spectroscopy (TOCSY) experiments unlocked the identification of smaller products from the substrate breaking. Thus, signals corresponding to dihydrosinapyl alcohol (DHSA), 4-propylsyringol (4-PSG) and guaiacol (GUAC) were identified. Obtention of DHSA and 4-PSG was confirmed by the appearance of the signals corresponding to hydroxypropyl and propyl chains, respectively (see SI, Figure S31). On the other side, GUAC was identified by the characteristic singlet of the methoxy group appearing at a lower field with respect to the signals of the other products. Structures proposed by NMR were further confirmed by GC-MS (m/z : 212.2, 196.0 and 123.7, respectively). The reader is referred to the SI for a more detailed view of the NMR elucidation (see SI, *Sections 2.2 and 2.3*). After properly assigning ^1H signals, quantification required recording routine ^1H NMR spectra at 298 K. For that purpose, around 0.35 g of the reaction mixture were mixed in an NMR tube with 0.35 g of an internal standard solution (0.3 wt.% hexamethyldisiloxane in THF-d_8). Deuterated solvent signals were used as chemical shift references.

Reusability tests for magnetically induced catalysis. Reusability tests with DPE as a model substrate were carried out for NiCo NPs. For catalyst recovery, after the reaction, the solid catalyst was separated inside the glovebox with the help of a magnet, washed 3 times with 5 mL of toluene (30 s washing) in the same reactor at room temperature, and then dried under vacuum. Afterwards, the solid catalyst was again used in a new catalytic reaction (re-use). The re-usability tests, including catalytic experiments together with the GC analyses, were performed in the same way as the common experiments with individual substrates already described.

RESULTS AND DISCUSSION

Compositional and Structural Characterization of NiCo NPs. NiCo bimetallic systems containing different Ni:Co ratios (Ni_5Co_5 , Ni_6Co_4 , Ni_7Co_3 , and Ni_8Co_2) have been prepared by the co-decomposition of $\text{Ni}[\text{PrNC}(\text{CH}_3)\text{N}^i\text{Pr}]_2$ and $\text{Co}[\text{N}(\text{SiMe}_3)_2]_2(\text{thf})$, in the presence of 0.04 eq. of PA ligand under mild conditions (120 °C, 3 bars H_2). This variety of molar ratios was selected based on previous work, resulting in a family of materials with various hydrogenation activities and magnetic properties. (43) The Ni:Co ratio determined by ICP was found to be very similar to the theoretical one in all cases, while the organic content was found around 20% by weight in each case, regardless of the nanoparticle metal composition. These results can be found in Table S1 of the Supporting Information.

The NiCo samples were characterized using bright field transmission electron microscopy (BF-TEM) working at 120 kV. The NPs, in all cases, display a homogeneous ellipsoidal shape with some surface

roughness and varying degrees of agglomeration throughout the grid. Actually, it is possible to find agglomerates and well-isolated NPs for every Ni:Co ratio. The size of the NPs was also determined by BF-TEM imaging, measuring the major axis of the ellipsoidal shape. NP distributions with a mean size of 13 nm are observed in all cases except for Ni₅Co₅, which shows slightly larger sizes centered around 16 nm. Interestingly, the compositions Ni₆Co₄, Ni₇Co₃ and Ni₈Co₂ are relatively monodisperse, while the composition Ni₅Co₅ shows broader size dispersity. Nonetheless, for all Ni:Co ratios, the nanoparticle size distributions are relatively uniform and can be modelled with a Gaussian function. This is common when using controlled synthesis methods, such as the organometallic approach. (44)

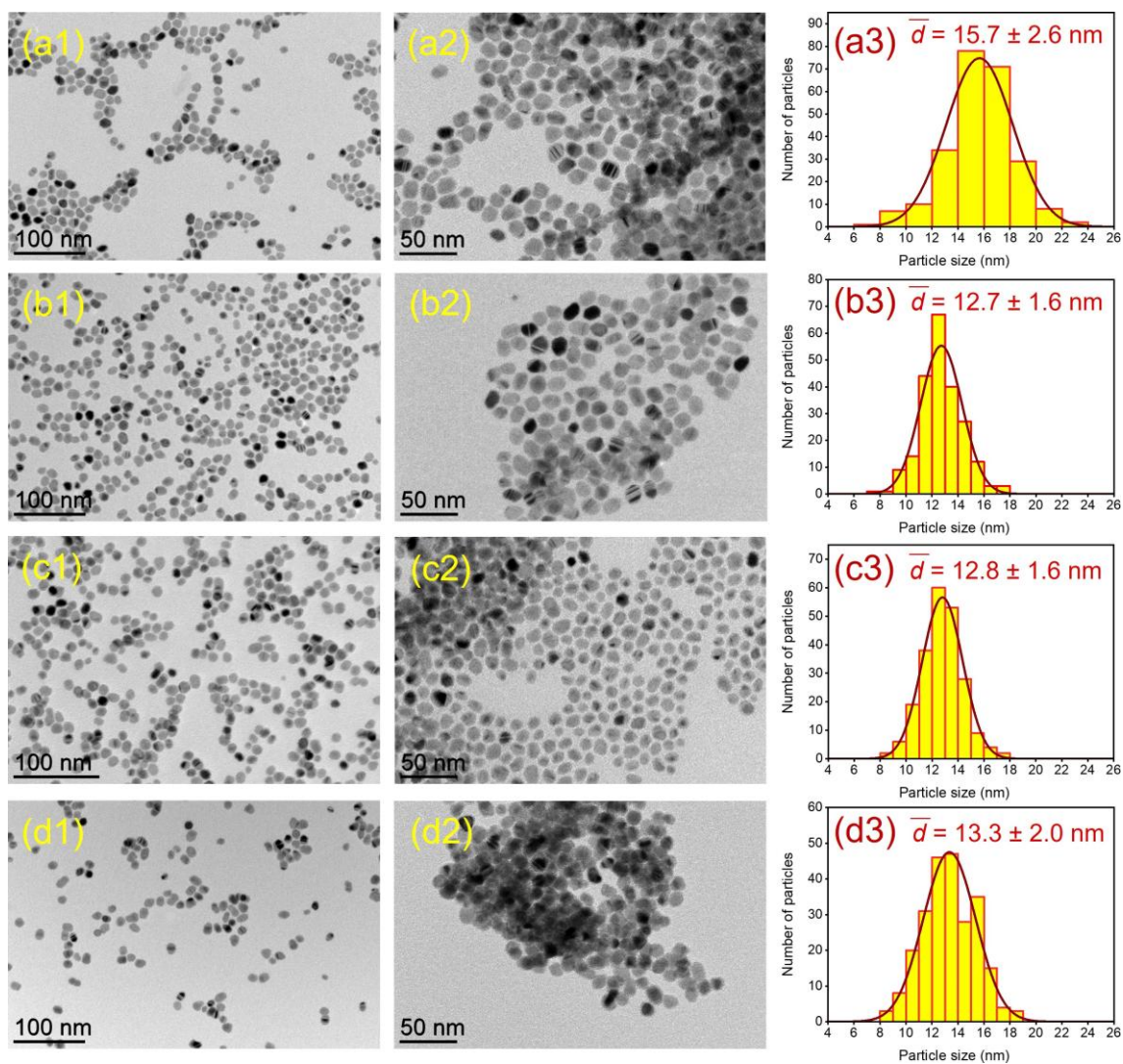


Figure 1. (1,2) BF-TEM micrographs of the NiCo-NPs synthesized with a variation of the Ni:Co molar ratios. (3) Particle size distributions considering a minimum of 200 nanoparticles. *a*: Ni₅Co₅, *b*: Ni₆Co₄, *c*: Ni₇Co₃, *d*: Ni₈Co₂.

In Figure 2, the combination of 200 kV HR-TEM and HR-STEM imaging for Ni₇Co₃, which will be the composition used in most catalytic studies, reveals a system composed of larger polycrystalline particles (≥ 10 nm), where some stacking defects are clearly visible, and smaller particles surrounding them (≥ 2

nm). Routine X-ray diffraction in reflection geometry allows for assigning a cubic structure to the larger NPs composing the core of the system (see SI, Figure S1). Additionally, STEM-EDX analysis was performed on all NPs to determine the metal distribution throughout the microstructure. Figure 2 (e-g) shows the results for Ni_7Co_3 . Remarkably, EDX corroborates a complex structure for the nano-objects, where there are larger particles composed mainly of Ni with smaller Co-rich particles around them. Interestingly, a high concentration of cobalt in the reaction medium would increase the size of the outer nanoparticle layers, which could explain why the composition with the highest Co content (Ni_5Co_5) has the largest average size (Figure 1a). This is consistent with the findings of Palazzolo *et al.* when using low Ni:Co ratios. (45) Analogous results were obtained for other compositions in HR-TEM, HR-STEM and STEM-EDX, with the images shown in the SI (Figures S12-S13). In agreement with these observations, the XANES spectra at Ni and Co K-edges of Ni_5Co_5 and Ni_7Co_3 samples can be found in Figure S12. A displacement on both edges confirms the intimate contact between the two metals in the bimetallic system. Additionally, the spectra at the Co K-edge can support the presence of Co in the external region of the bimetallic particle, where the increase in the white line of the Ni_7Co_3 composition can perceive some oxidation of Co atoms. This oxidation is only seen for Co, which could indicate that these metallic atoms are more prone to be oxidized by adventitious air with respect to Ni, which would be at the center of the bimetallic system.

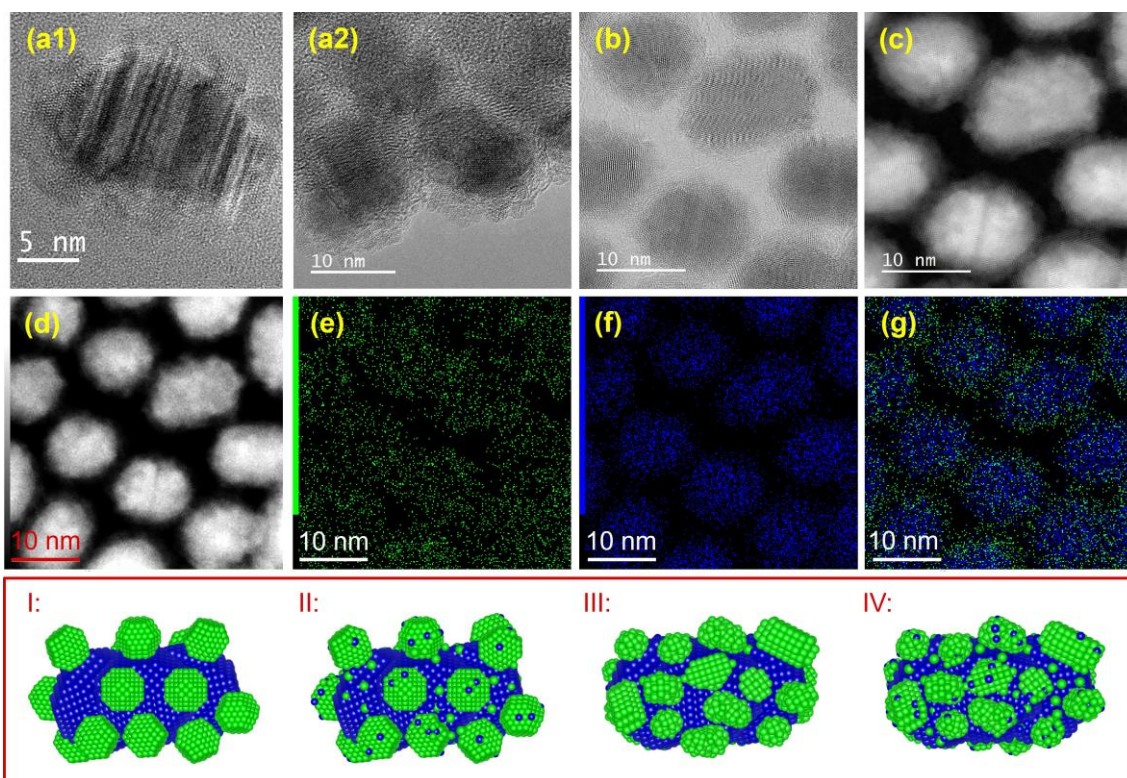


Figure 2. Ni_7Co_3 -NPs. *Top:* (a) HR-TEM images, (b) HR-STEM-BF image, (c) HR-STEM-HAADF image, (d) STEM-HAADF image and corresponding (e)–(g) STEM-EDX elemental maps showing Ni in blue and Co in green and overlap of Ni and Co maps. *Bottom:* plausible structural models in agreement with HR-EM observations.

However, after the HR-EM measurements, some doubts still arose about the true nature of the bimetallic system. In the first place, it was uncertain whether the core of the system consists of pure large Ni NPs with small pure Co NPs (or sub-nanometric clusters) surrounding them, or if both parts of the system are alloys, each richer in one metal but doped with the other. In fact, under our reaction conditions, Ni and Co are miscible, which means that the formation of a cobalt-nickel gradient in the NP top layers is possible. (46) Then Co can crystallize in the face-centered cubic (fcc) and hexagonal close-packed (hcp) structures above or below 420 °C, respectively. Still, both Co phases can be stabilized at room temperature (within a broad range of particle sizes), depending on specific synthesis conditions. (47) Moreover, recent theoretical studies have shown that the stability of small Co clusters ($N_{\text{Co}} \approx 55-5500$) is higher in the icosahedral shape, (48-50) which may be considered as a distortion of a regular cuboctahedron with an fcc stacking. According to this reasoning, four plausible models believed to be compatible with HR-TEM results have been added to Figure 2. In all cases, polycrystalline NPs adopting a cubic structure characteristic of Ni have been selected as the core. The model I corresponds to a situation involving fcc Co NPs following a truncated octahedron pattern. The truncated octahedral shape has been chosen to mimic the spherical shape of the NPs observed by HR-EM, but a cuboctahedron or even an icosahedron (non-crystalline) may also be feasible at this stage. Model II is a similar situation but with some Co doping in the Ni-rich NPs and vice versa. On the contrary, models III and IV both adopt an hcp structure characteristic of Co but differ in the presence of doping of Ni into Co and Co into Ni in Model IV. Obviously, there could be potential intermediate situations at this point.

In order to differentiate between these scenarios, high-quality XRD data was obtained in transmission geometry and Rietveld refinement was applied to determine the most suitable fit. In the same direction as routine XRD, the XRD diagram acquired in transmission geometry reveals that a single fcc pattern with a lattice parameter close to that of the fcc-Ni structure (1434892.cif file) could index all the main peaks observed. However, a small shoulder that can be observed at the left of the most intense peak (around 20°) is not indexed by a single fcc structure. Further investigations reveal that this shoulder can be reproduced through the addition of the hexagonal Co phase, as described in the 9008492.cif file. Rietveld refinement of the diagram has therefore been attempted using the fcc-Ni and hcp-Co phases in the model (Figure S2). All phases are modelled as showing isotropic crystallites, the size of which is refined. For each phase, the phase fraction and lattice parameters were also refined. Such a model ($R_{\text{wp}} = 9.78$) provided crystallite sizes close to TEM observations, but the phase fractions did not align with what was expected, considering the metal contents estimated by ICP. A closer look reveals that some peaks are not fully described by the model (Figure S2); therefore, the cubic phase of Co (1534891.cif file) was added to the model (Figure S3). Interestingly, although this hypothesis of 3 phases (Co-hcp, Co-fcc, Ni-fcc) did not significantly improve the fitting ($R_{\text{wp}} = 9.43$), the fractions of cobalt and nickel were approaching the expected values. Consequently, we carried out a final simulation using a Ni-Co alloy with the fcc structure as the model (Figure 3 and S4). For that purpose, we used the Ni fcc structure as a basis and added some disorder on the Ni site (0,0,0 site), this site being shared by Ni and Co atoms (total occupancy of this site being constrained to 1). We found that cubic Ni being actually a solid solution of

Ni and Co ($\text{Ni}_6\text{Co}_3\text{Co}_3$), with 10 nm particles, completed by a 1.9 nm hexagonal Co, improved the fitting considerably ($R_{\text{wp}} = 8.47$). Additionally, the possible presence of CoO, which would also give a main peak at around 20° was checked (Figure S5). In that case, the addition of CoO (1533087.cif file) in the refinement did not improve the results. Moreover, the phase fraction of CoO after refinement converges to zero. Nevertheless, analyzing the data is challenging due to several factors: the mixture of large Ni-rich particles and ultrasmall Co-rich particles that diffract at similar angles, the nanometric size of Co particles, the coincidence of Co and Ni scattering peaks, and the presence of around 20 wt.% of PA. Therefore, the results of these Rietveld analyses must be treated with considerable caution.

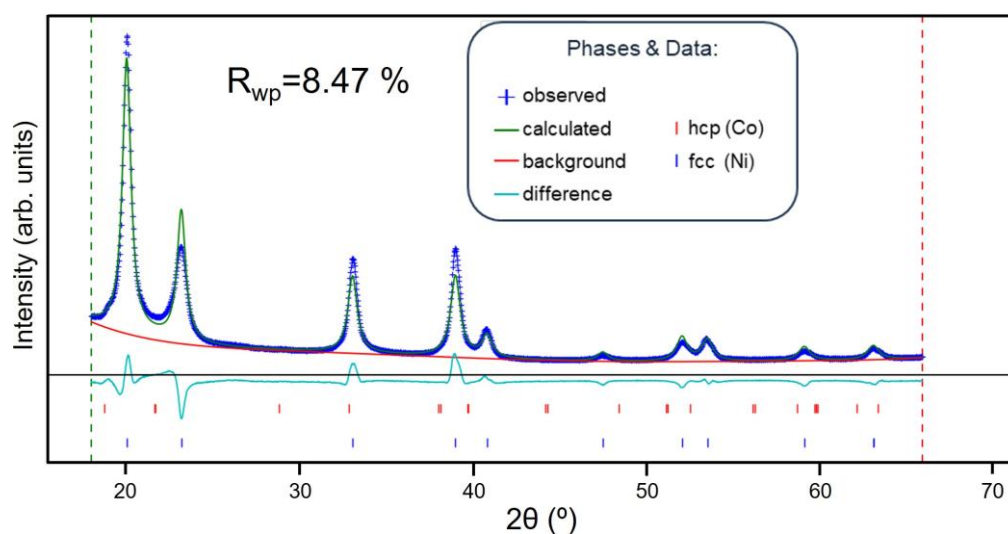


Figure 3. Rietveld refinement of the XRPD pattern of Ni_6Co_4 -NPs. (Ni: 1534892.cif, Co: 9008492.cif)

Another important fact to be considered is that the electron beam interaction causes size changes in the small Co-rich NPs during image acquisition. A little growth of the small NPs decorating the big ones is observed. Besides that, it is possible that the larger hexagonal Co NPs causing diffraction phenomena are the only ones being detected by XRD analyses. All this makes it difficult to accurately judge their size using previous techniques. However, by making a hypothesis on the shape of the nanoparticle and having a system with a narrow particle size distribution, it is possible to estimate an average nanoparticle size by using the coordination number of the first shell of metallic NPs obtained by EXAFS fittings. Figure 4 shows the moduli of the Fourier Transform of NiCo-NPs spectra, while Table 1 summarizes the structural parameters of NiCo-NPs obtained through EXAFS data analysis. By using the coordination number (51) for the estimation of a cuboctahedral NP size (where Co also shares Co-Co distances and neighbouring atoms as in the hcp structure), the $N_{\text{Co-Co}} = 4.6$ in the Ni_5Co_5 sample results in an average nanoparticle size of ~ 0.7 nm, which must be considered as an average Co cluster size in the entire system. Additionally, the coordination numbers obtained for the NPs in both Ni and Co edges are in good agreement with the results obtained by electron microscopy, pointing out that the Ni_5Co_5 system is composed of larger NPs in comparison to Ni_7Co_3 . The analysis of the latter sample showed some oxidation of Co atoms (see arrows in Figure 4b), the presence of which renders a specific size

estimation for the smaller Co-rich NPs difficult in this case. EXAFS modelling points to this oxidation being compatible with the presence of CoO.

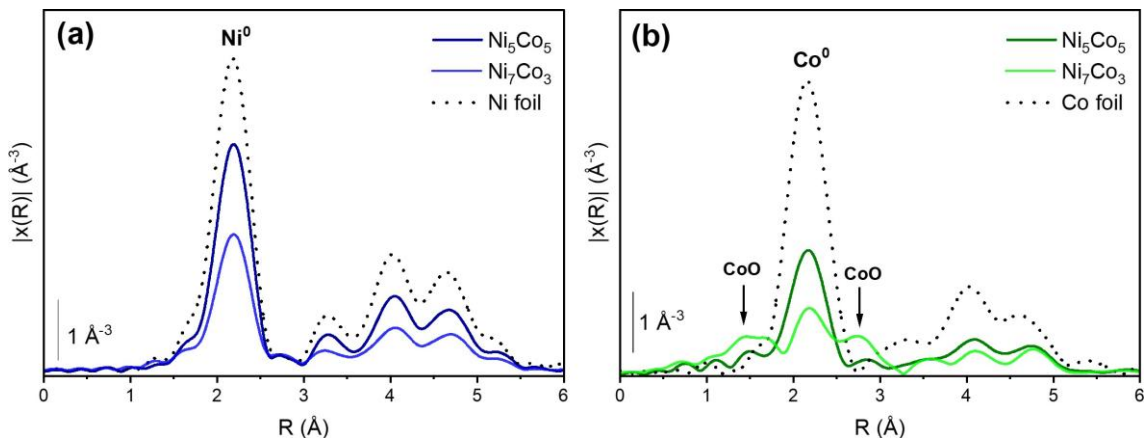


Figure 4. k^2 -weighted Moduli of Fourier Transform of NiCo-NPs at Ni (a) and Co (b) K-edges.

Table 1. Summary of EXAFS fits of NiCo-NPs samples.

Sample	N	Path	R (Å)	σ^2 (Å ²)	ΔE_0 (eV)	r-factor (%)
Co K-edge						
Ni ₅ Co ₅	4.6 ± 1.0	Co-Co	2.491 ± 0.015	0.0049 ± 0.0019	7.8 ± 2.7	0.0404
	2.7 ± 0.8	Co-O (CoO)	2.059 ± 0.025	0.0096 ± 0.0062		
Ni ₇ Co ₃	2.6 ± 0.7	Co-Co (Co ⁰)	2.490 ± 0.014	0.0064 ± 0.0022	7.8 ± 1.8	0.0499
	2.4 ± 0.7	Co-Co (CoO)	3.012 ± 0.021	0.0064 ± 0.0022		
Ni K-edge						
Ni ₅ Co ₅	6.3 ± 0.4	Ni-Ni	2.487 ± 0.004	0.0052 ± 0.0004	8.3 ± 0.6	0.0018
Ni ₇ Co ₃	3.8 ± 0.2	Ni-Ni	2.482 ± 0.003			0.0127

^aThe fits on the Ni K-edge were performed in the first coordination shell over FT of the k^2 -weighted $\chi(k)$ functions performed in the $\Delta k = 2.0$ -13.5 Å⁻¹ and $\Delta R = 1.4$ -2.8 Å intervals for completely reduced samples. The fits on the Co K-edge were performed up to the second coordination shell over FT of the k^2 -weighted $\chi(k)$ functions. For the completely reduced sample, the fit was performed in the $\Delta k = 2.0$ -12.0 Å⁻¹ and $\Delta R = 1.4$ -2.8 Å intervals, while in the oxidized one, the fit was performed over $\Delta k = 2.0$ -12.0 Å⁻¹ and $\Delta R = 1.0$ -3.5 Å intervals. S_0^2 (Ni) = 1.0, S_0^2 (Co) = 0.74.

From the combination of all these analyses, the presence of large cubic Ni particles is clear, which are likely doped with Co and decorated by smaller Co particles (≤ 2 nm) mostly crystallized in the hexagonal phase. Finally, mixed structures of fcc and hcp Co with stacking faults cannot be ruled out for the smaller NPs.

Magnetic and calorimetric characterization of NiCo NPs. The magnetic properties of the NiCo-NPs were determined by vibrating sample magnetometry, (VSM; Figure S8). At 300 K, the hysteresis cycle

measured for Ni₅Co₅-NPs is characteristic of a ferromagnetic material, with a saturation magnetization (M_S) of 115 A·m²·kg⁻¹, a remnant magnetization (M_R) of 14 A·m²·kg⁻¹ and a coercive field (μ_0H_C) of 18 mT, values that came close to those reported for much larger NiCo anisotropic structures. (52) Interestingly, Margeat *et al.* reported large values of M_S for small Co NPs (\approx 3 nm), where hcp structures were also identified. (53) Also, the high coercivity found can be tentatively ascribed to highly anisotropic small Co-hcp NPs decorating the larger Ni-rich nanoparticle, as seen by other authors in 2 nm Co NPs implanted on SiO₂. (54) Nonetheless, long-range order effects on the MagNPs in the presence of the magnetic field, whose study is beyond the scope of this work, may also account for these observations. (55)

As expected, upon increasing the amount of Ni, the coercivity values decrease, until showing a saturation magnetization value of 77 A·m²·kg⁻¹, a remnant magnetization of 2 A·m²·kg⁻¹ and a coercive field of 5 mT at 300 K for the Ni₈Co₂ sample (Table 2), showing a behaviour getting closer to superparamagnetic. This fact is even more evident in the analyses carried out after cooling down to 5 K (Figure S8). Additionally, there was no sign of exchange bias in any case, thus pointing to the absence of oxidation.

Table 2. Magnetic properties and SAR values of Ni_{10-x}Co_x-NPs.

Material	M_S (A·m ² ·kg ⁻¹) ^a	M_R (A·m ² ·kg ⁻¹) ^a	H_C (mT) ^a	SAR (at 93 kHz, 49 mT) (W·g ⁻¹) ^b
Ni ₅ Co ₅	115	14	18	513
Ni ₆ Co ₄	99	3	3	492
Ni ₇ Co ₃	91	3	4	310
Ni ₈ Co ₂	77	2	5	126

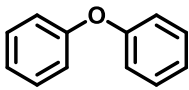
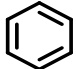
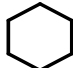
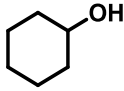
^a Measured at the 300 K. ^b SAR values are normalized with respect to the metal content in the sample.

In the same line, the SAR measurements (Figure S10) show that the hyperthermia properties of these NPs present a clear compositional dependence. The SAR measured for the Ni₅Co₅-NPs indicates they get activated at high magnetic fields, around 30 mT, while the value obtained at the maximum coil power (working at 93 kHz) is 513 W·g⁻¹. For Ni₆Co₄, we can already observe the effect of the higher presence of Ni in the SAR plot. These NPs get activated at 24 mT, and the SAR value obtained at 48 mT is 492 W·g⁻¹, which lies close to the Ni₅Co₅ composition. As an effect of the even higher presence of Ni, the Ni₇Co₃-NPs start heating at low magnetic fields (19 mT), but in this case, we already observe a remarkable decrease in the SAR values. At the maximum field, only 310 W·g⁻¹ are achieved. Last, when we reach the composition with the highest quantity of Ni (Ni₈Co₂), the NPs get activated at very low fields (10 mT). However, the heating power decreases quite significantly, the SAR value at 49 mT being only 126 W·g⁻¹.

All these observations evidence the magnetic hardness and softness provided by Co and Ni, respectively, to the composition. With high Co contents, the NPs are less influenced by the external magnetic field, but once activated, they retain magnetization, thus creating large hysteresis loop areas and significant hysteresis losses that translate into high heating powers (i.e., high SAR values). Conversely, with high Ni contents, the NPs can be easily magnetized and demagnetized, with very low coercivity and low hysteresis losses. Therefore, these materials generate less heating (i.e., low SAR values), but start heating at lower fields.

Initial catalytic tests with DPE. After extensively analyzing the chemical and physical features of the NiCo family, we first decided to test them in the DPE reaction under hydrogen (Table 3). This reaction helps us gauge the catalytic activity for the C–O bond cleavage, which is a suitable indicator of the heating power of the NPs, and a crucial step in lignin depolymerization. Typically, 1 mmol of DPE was dissolved in 5 mL of decane together with 8 mg of NiCo-NPs (around 10 mol% with respect to the substrate DPE). The experiments were conducted for 8 h and carried out under 3 bars of H₂ and applying 50% of the power of a 300 kHz coil (6.6 kW, 39 mT).

Table 3. Catalytic tests under MI with NiCo-NPs and DPE as a preliminary model substrate.

Material (NPs)	 DPE conversion (mol.%)	 Benzene yield (carbon basis, mol.%)	 Cyclohexane yield (carbon basis, mol.%)	 Cyclohexanol yield (carbon basis, mol.%)
Ni ₅ Co ₅	38	18	1	14
Ni ₆ Co ₄	86	36	3	34
Ni ₇ Co ₃	100	34	13	47
Ni ₈ Co ₂	30	10	3	12

R. conditions: Batch-type reactor, 1.0 mmol DPE, 0.7 mmol dodecane, 5 mL decane, 8 mg cat (≈ 0.1 metallic mmol), AMF 300 kHz, 39 mT, 3 H₂ bar, 8 h. Note: Only traces of dicyclohexylether and cyclohexylphenylether could be detected.

After carrying out the reaction with all the different NiCo ratios prepared (Table 3), we realized the Ni₅Co₅ and the Ni₈Co₂ samples did not lead to satisfactory results at the studied reaction times, probably lacking catalytic properties in the former case, and heating power in the latter. On the contrary, the Ni₆Co₄ and the Ni₇Co₃ compositions were both perfectly capable of transforming DPE, the Ni₇Co₃ being somewhat more active than the Ni₆Co₄ in the C–O cleavage (≈ 100 vs $\approx 86\%$ cleavage) and considerably more prone to aromatic ring hydrogenation (mol ratio cyclohexanol/benzene: 0.38 vs 0.08). This lower

tendency to hydrogenate the aromatic rings of the Ni₆Co₄-NPs may be quite promising for specific applications. Nonetheless, once the stability of the compositions was assessed, we found for the Ni₇Co₃ that, although the material gets agglomerated, the NPs largely preserve their shape and size (Figure S42). Conversely, the BF-TEM imaging reveals how, when subjecting the Ni₆Co₄ composition to the reaction conditions, the average size of the NPs significantly increases, up to the observation of coalescence phenomena (Figure S43). Indeed, the temperature registered with the IR camera during the reaction for the Ni₆Co₄ catalyst was higher than that observed for the Ni₇Co₃ composition (≈ 150 vs. 120 °C). This temperature difference could be a reason for the coalescence of Ni₆Co₄ NPs.

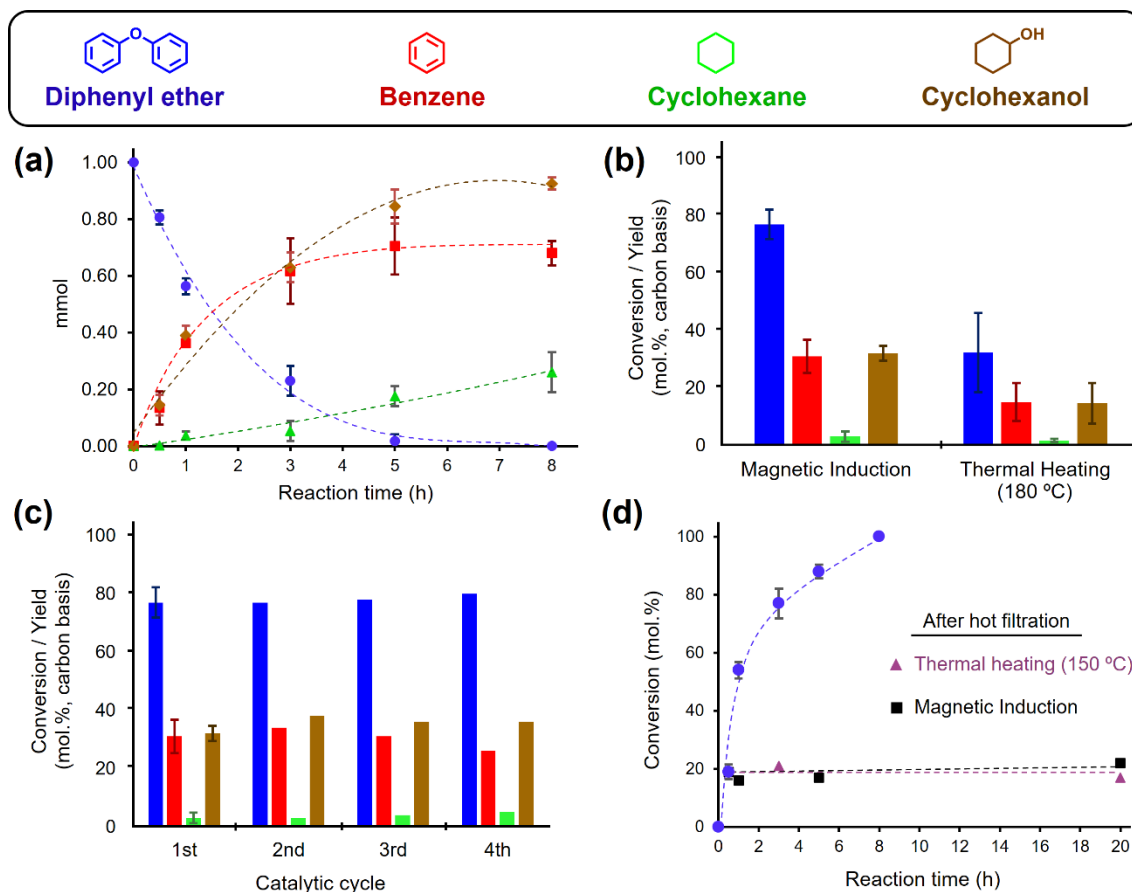


Figure 5. Catalytic performance of Ni₇Co₃-NPs in DPE hydrogenation under MI. (a) Temporal evolution of product distribution; (b) Comparison against conventional heating with analogous reaction conditions; (c) Catalyst reusability after washing with toluene; (d) Hot filtration tests. Reaction conditions: Batch-type reactor, 1.0 mmol DPE, 0.7 mmol dodecane, 5 mL decane, 8 mg cat (≈ 0.1 metallic mmol), AMF 300 kHz, 39 mT, 3 H₂ bar. In (b) and (c), reaction time has been adjusted to 3 hours to keep conversion below 80%. Notes: ⁱ⁾ Dashed lines intend to serve only as visual guidelines. ⁱⁱ⁾ Error bars correspond to the standard deviation of at least 2 repetitions of the same catalytic test.

Figure 5 summarizes the temporal evolution of product distribution (a), comparison against conventional heating (b), hot filtration test (d) and reusability of the Ni₇Co₃ catalyst (c). The graphical representation of the product distribution over time, as shown in Figure 5a, reveals the marked absence of hydrogenation products such as cyclohexylphenyl ether (CPE) and dicyclohexylether (DCE). The

presence of this trend is a clear indication of the preference of the catalyst to cleave C-O bonds before initiating the hydrogenation process of the aromatic rings. Moreover, it is remarkable that no phenol was detected, revealing the formation of a possible partially hydrogenated intermediate, specifically cyclohexylphenylether, evolving towards cyclohexanol and benzene. To verify this, additional experiments with Ni₇Co₃-NPs were conducted at short reaction times to determine the initial reaction rates for phenol, cyclohexanol, benzene, CPE, and DPE (only C-O cleavage) as individual substrates (see Table S5). While there was no reactivity for CPE, the activity for DPE ether cleavage (**3.4 min⁻¹**) and cyclohexanol hydrogenation (**4.3 min⁻¹**) was lower than that of benzene hydrogenation (**5.4 min⁻¹**) and much lower than that of phenol hydrogenation (**7.9 h⁻¹**). This suggests that the preferred reaction pathway does not involve the generation of the partially hydrogenated molecule (CPE). Instead, the reaction occurs through the breaking of the DPE C-O bond and a rapid hydrogenation of phenol into cyclohexanol, with a slower conversion of benzene into cyclohexane. This mechanism was also observed in our previous studies with FeNi₃-based NPs under magnetic induction and similar H₂ pressures. (11) The cleavage of one DPE molecule generates, in the first stage, one hydroxylated molecule and one cyclic hydrocarbon, thus the ratio (benzene + cyclohexane)/(phenol + cyclohexanol) close to the unity observed at all times indicates low to zero selectivity to HDO after ether bond cleavage, (56), which, in turn, reflects the catalyst's inability to execute the following reaction sequence: phenol → cyclohexanol → cyclohexene → cyclohexane. As expected, the lack of significant acidity in our purely metallic catalysts prevents the cyclohexanol dehydration to cyclohexene.

Interestingly, the conventional heating tests displayed in Figure 5b offer compelling evidence that the temperature on the surface of the NPs is significantly higher than the temperature recorded by the Infrared camera on the bulk surface (120 °C). This was evident from the comparison of these reactions carried out at 180 °C using conventional heating and magnetic induction, where the latter showed a significantly higher conversion level (77 vs. 32 mol.%). Moreover, after performing a hot filtration and placing the reaction mixture in both the coil and a 150 °C oil bath, the results showed no significant leaching of magnetic and/or catalytically active species (Figure 5d). In the same line, no cobalt leaching was identified in the reaction mixture after 8 hours by ICP analysis. Only a minor amount of nickel was present (<2 wt%, Table S7). This confirms the true heterogeneous nature of the catalytic phenomena and, together with the preservation of the Ni₇Co₃ nanoparticle size and shape (Figure S42), explains the good reusability of the material seen in Figure 5c.

Catalytic tests with lignin-linkage models. Inspired by the promising catalytic results obtained with Ni₇Co₃-NPs on DPE hydrogenolysis, the applicability of this catalyst was tested under optimal reaction conditions on different types of lignin linkage model compounds, including β-O-4 (2-phenoxy-1-phenylethanol), α-O-4 (4-benzyloxyphenol), and 4-O-5 (4-phenoxyphenol) (Figure 6). Relevantly, linkage models with hydroxyl groups were preferred over systems only containing ether functions because they were considered to be closer to the situation the catalyst would be facing against the real lignin molecule.

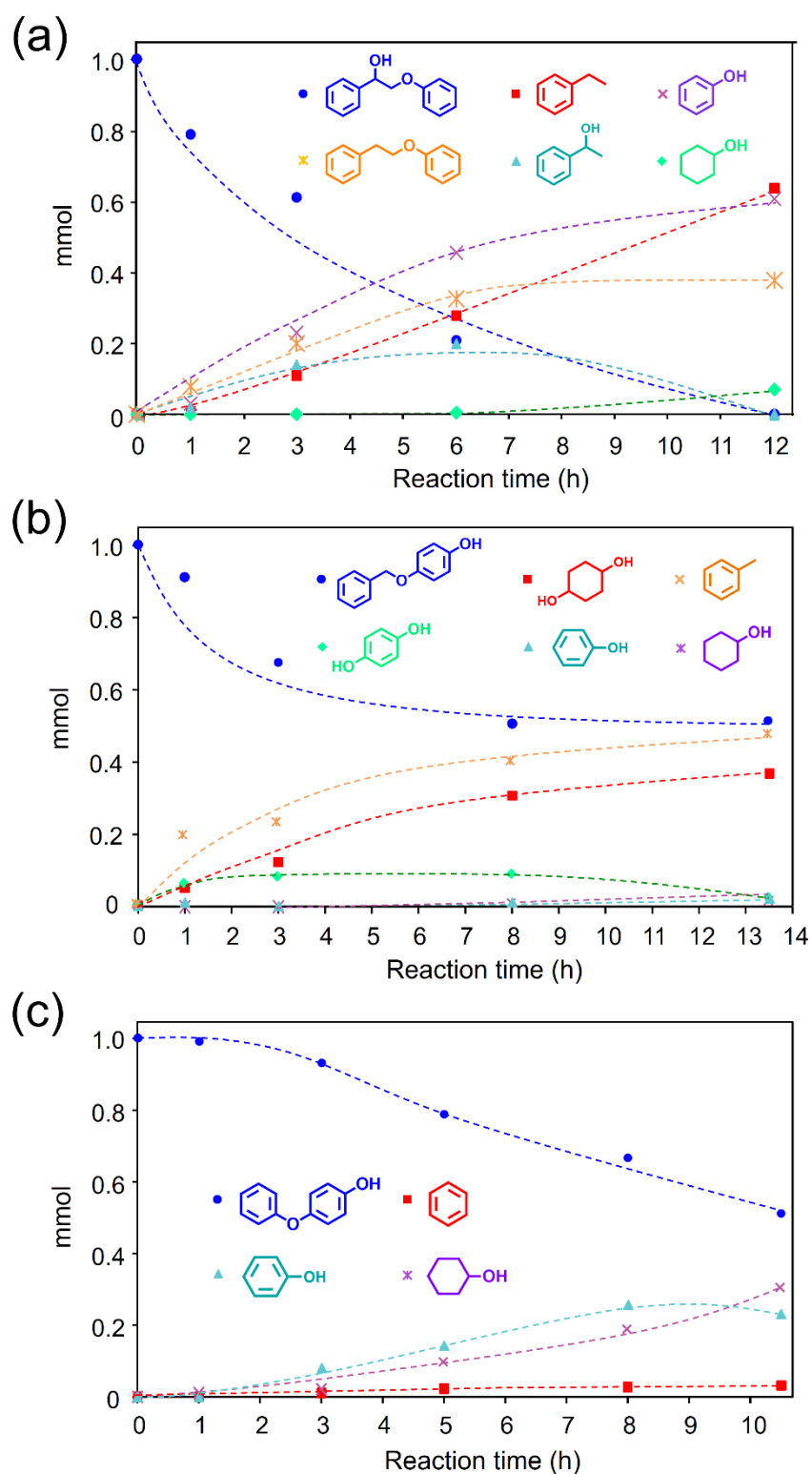


Figure 6. Kinetic profiles for different lignin linkage models treated with Ni_7Co_3 -NPs, H_2 , and MI: (a) 2-phenoxy-1-phenylethanol (β -O-4), (b) 4-benzyloxyphenol (α -O-4), (c) 4-phenoxyphenol (4-O-5). Reaction conditions: Batch-type reactor, 1.0 mmol substrate, 0.7 mmol dodecane, 5 mL solvent (2-phenoxy-1-phenylethanol: 1 mL decane + 4 mL THF; 4-benzyloxyphenol and 4-phenoxyphenol: 3 mL decane + 2 mL THF), 8 mg cat (≈ 0.1 metallic mmol), AMF 300 kHz, 65 mT, 3 H_2 bar. Notes: ⁱ⁾ Dashed lines intend to serve only as visual guidelines. ⁱⁱ⁾ Carbon balances at the longest reaction times were above 90% in all cases.

In Figure 6, it can be observed that no substrate could be converted with a 100% C–O bond cleavage, indicating that it will be difficult for the Ni₇Co₃-NPs to be successful at completing the lignin depolymerization. In the case of 2-phenoxy-1-phenylethanol, the cleavage of the C–O bond stops at ≈60 mol.%, a constant concentration of 2-phenethyl phenyl ether being observed beyond that point. In both 4-benzyloxyphenol and 4-phenoxyphenol, conversions above 50% are difficult to attain. Especially significant is the case of 4-phenoxyphenol, which shares a very similar molecular structure with diphenyl ether, the only difference being the presence of a hydroxyl group (–OH) in the para position on one of the phenyl rings in 4-phenoxyphenol. The difference in activity between 4-phenoxyphenol (**0.1 min⁻¹**) and diphenyl ether (**4.0 min⁻¹**) after one hour of reaction was more than an order of magnitude, as revealed by their respective TOFs. Although one could think that an electron-donating group may weaken the C–O bond by increasing the electron density around the oxygen atom, making the carbon more nucleophilic and susceptible to attack, the previous section also unravelled the preference of the catalyst to react with phenol (see also Table S5). Therefore, it is possible to tentatively attribute the cause of the decrease in catalytic activity to the competition between –OH groups and C–O bonds for the active site. In fact, small amounts of certain products where either the aromatic systems are partially hydrogenated, or the –OH removed, while the C–O bonds are still preserved, were also observed during the catalytic tests (i.e., 2-phenethyl phenyl ether, benzyloxybenzene, 4-cyclohexyloxyphenol).

Catalytic tests with lignin-oil molecules. It is well known that after lignin depolymerization, the liquid fraction known as lignin oil or bio-oil possesses relatively low energy density due to the rich oxygen content. As previously said, it must be submitted to an upgrading treatment to remove oxygen, usually involving a catalytic hydrodeoxygenation (HDO) process. (26,27) Therefore, to assess the effectiveness of Ni₇Co₃-NPs in lignin oil upgrading, important constituents of lignin oils from specific depolymerization methods were chosen, including guaiacol (in fast pyrolysis and acid depolymerization), vanillin (in alkaline lignin oxidation), and m-cresol (in harsh hydroprocessing). (23) Additionally, anisole, a methoxy-rich lignin compound, and eugenol, a minority compound valued as a probe for lignin monomer units (p-coumaryl, sinapyl, and coniferyl alcohols), were also included in this selection. This set of model compounds comprises the most representative chemical functions found in lignin and compounds derived from it, including aromatic rings, hydroxyl groups, keto groups, and ether linkages.

Table 4. Catalytic tests under MI with Ni₇Co₃-NPs and different lignin oil model compounds.

Reaction time (h)	Substrate (conversion)	Main Products (yield mol.%, carbon basis)	Field (mT)
8	(100)	(88)	65
11	(100)	(85) (17)	39
45	(100)	(85) (4)	39
45	(80)	(53) (5)	65
48	(100)	(83) (5)	39

Reaction conditions: Batch-type reactor, 1.0 mmol substrate, 0.7 mmol dodecane, 5 mL solvent (vanillin, m-cresol, guaiacol: 3 mL decane + 2 mL THF; anisole, eugenol: 5 mL decane), 8 mg cat (≈ 0.1 metallic mmol), AMF 300 kHz, 3 H₂ bar. Note: Complete kinetic profiles can be found in the SI (Section S3.3).

The first entry of Table 4 shows how vanillin can be selectively transformed into 2-methoxy-4-methylphenol (MMP), a flavoring agent and a potential biofuel. (57) However, it is challenging to remove the methoxy group in vanillin at low H₂ pressures using a catalyst that lacks specific oxygen adsorption centers, such as acid sites or oxygen vacancies. Conversely, anisole (second entry) presents a high degree of demethoxylation which, according to the reaction kinetics (Figure S35), seems to proceed mostly via direct deoxygenation to benzene. This mechanism (58) suggests that the temperature of the NPs during reaction is probably close to 300 °C. In the third entry, only the aromatic ring of m-cresol could be reduced. Direct deoxygenation would require specific adsorption sites located at metal/oxide interfaces. (59) On the other hand, the dehydration of 3-methylcyclohexanol seems difficult in the absence of acidity, as seen when studying the reactivity of DPE-derived cyclohexanol. In the same line, eugenol (last entry) could get demethoxylated and hydrogenated but barely deoxygenated (i.e., removal of the -OH). Nonetheless, it is worth mentioning that the absence of 2-methoxy-4-propylcyclohexanol in the kinetic profile (Figure S38) points towards a mechanism where, first, the cleavage of the C_{aryl}-OCH₃

bond takes place through hydrogenolysis, and then the saturation of aromatic ring through hydrogenation. This prevailing mechanism is also seen in guaiacol (fourth entry) since no 2-methoxycyclohexanol was detected. It is important to note that this pathway does not require breaking any C_{alkyl}-OCH₃ bonds, which makes the catalyst advantageous for producing cyclohexanols from ortho-substituted monomethoxyphenols. (60) In summary, the reactivity of the Ni₇Co₃ sample towards this set of compounds indicates good activity for aromatic ring hydrogenation as well as for demethoxylation of ortho-substituted monomethoxyphenols. On the contrary, the catalyst is unable to perform more complex deoxygenations, such as -OH removal from phenol and cyclohexanol dehydrations, due to the lack of the required oxygen adsorption sites and acidity. In that sense, the use of support materials for the nanoparticles may constitute an interesting alternative to influence the electronic properties of the catalyst, and provide acid-base functionalities, thus affecting its performance in deoxygenation reactions. Surface functionalities or modifiers, such as partially oxidizing the surface of the nanoparticles or combining it with sulfides, could also be explored to alter the catalytic properties.

Decoration with Ru and enhancement of the C–O cleavage. During previous catalytic tests, it was found that the Ni₇Co₃ composition did not have the optimal balance of magnetic and catalytic properties to effectively break down C–O bonds in lignin linkage models. Therefore, it was decided to enhance the catalytic activity of Ni₇Co₃-NPs by decorating them with ruthenium, which is known for its ability to achieve high yields of phenolic monomers during the reductive fractionation of lignin. (61) For that purpose, a very small amount of Ru was added to Ni₇Co₃ NPs through low-temperature decomposition of Ru(COD)(COT) in the presence of H₂.

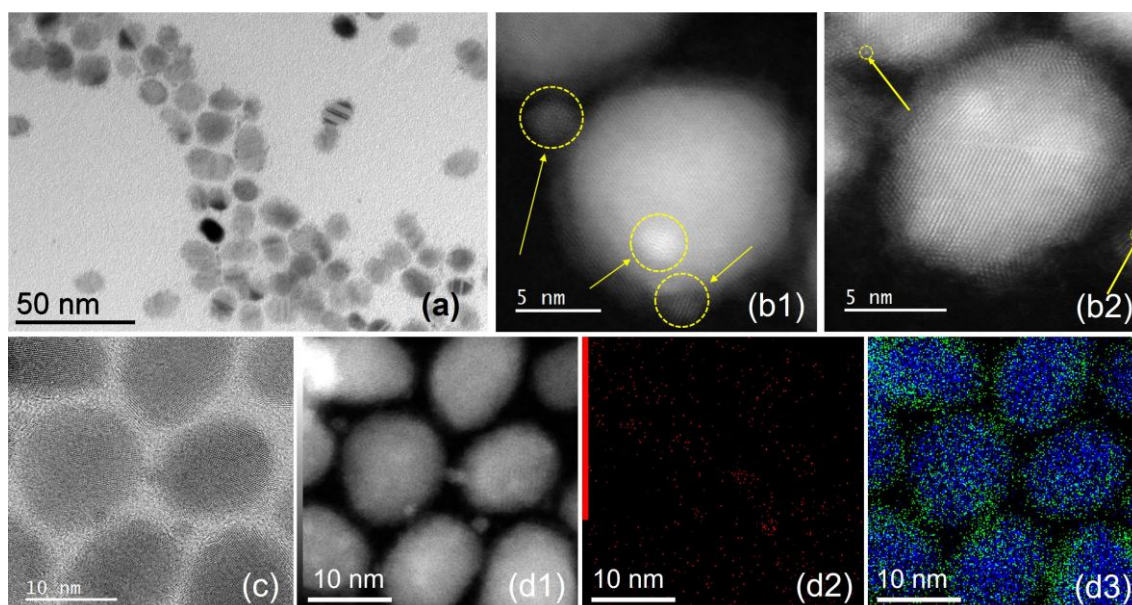


Figure 7. Ni₇Co₃@Ru-NPs: (a) BF-TEM image, (b) HR-STEM-HAADF image, (c) HR-STEM-BF image, (d) STEM-HAADF image and corresponding (d1)–(d2) STEM-EDX elemental maps showing Ru in red, Ni in blue, and Co in green.

Interestingly, ICP tests (Table S1) for the materials herein decorated revealed the amount of Ru incorporated was around 1 wt.%. Figure S7 shows how the crystalline structure of the parent Ni₇Co₃ sample is well preserved after the Ru incorporation. Also, no sign of the Ru species could be identified, meaning a successful dispersion of Ru species on the Ni₇Co₃ NPs. On the other hand, HR-EM measurements summarized in Figure 7 revealed the presence of several species on the Ni₇Co₃-NPs, identified with EDX to be Ru NPs and subnanometric clusters. Moreover, certain bright dots in the outer shell of the Ni₇Co₃ NPs, where some oxidation is expected to enhance the contrast, may be compatible with the occurrence of Ru single atoms (Figure 7; (b2)). In summary, the Ru decoration resulted in a “cocktail” of different Ru species, ranging from 2 nm NPs to subnanometric clusters or even isolated Ru atoms.

Figure 8 clearly shows that this minimum amount of Ru (≈ 1 wt.%) was enough to enhance C–O cleavage and improve catalyst prospects for lignin depolymerization. It is interesting to note that the level of improvement varies depending on the type of lignin connection, this increment being between 10 and 20 points in the case of the β -O-4 (2-phenoxy-1-phenylethanol) and 4-O-5 (4-phenoxyphenol), but almost twofold (45 vs. 88 mol.%) in the case of the α -O-4 model compound (4-benzyloxyphenol). As expected, the presence of Ru NPs also enhances the hydrogenation of aromatic rings, as shown in Figures S37-S39, where a more detailed comparison can be found.

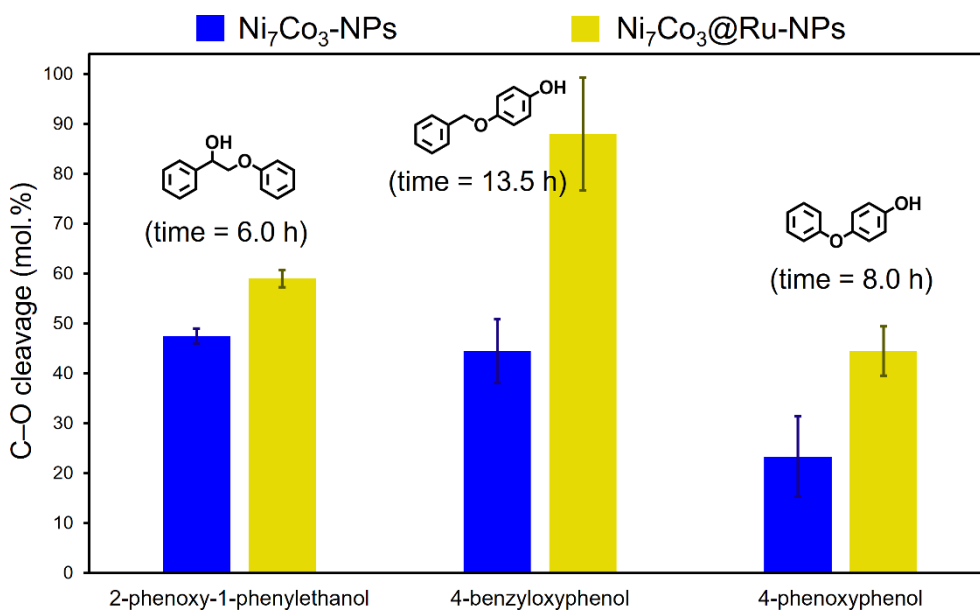


Figure 8. Comparison between Ni₇Co₃ and Ni₇Co₃@Ru NPs in the cleavage of several lignin linkage model compounds. Reaction conditions: Batch-type reactor, 1.0 mmol substrate, 0.7 mmol dodecane, 5 mL solvent (2-phenoxy-1-phenylethanol: 4 mL THF + 1 mL decane; 4-benzyloxyphenol and 4-phenoxyphenol: 2 mL THF + 3 mL decane), 8 mg cat, AMF 300 kHz, 65 mT, 3 H₂ bar. Notes: ⁱ⁾ C–O cleavage was calculated as the yield on carbon basis of all the products identified coming necessarily from this transformation. ⁱⁱ⁾ Carbon balances were above 90% in all cases. ⁱⁱⁱ⁾ Error bars correspond to the standard deviation of at least 2 repetitions of the same catalytic test.

The assignment of specific activities to individual Ru species within our catalyst is a highly intricate task. The Ni₇Co₃@Ru catalyst is composed of a mixture of clusters, nanoparticles, and single atoms, rendering it challenging to isolate and attribute individual contributions. Recent observations have indicated that the size of Ru particles significantly impacts their activity. Smaller Ru particles exhibit more significant activity in the C—O cleavage, which has been attributed to the higher number of edges and steps in smaller particles which, in turn, lowers the barriers to the cleavage of both C_{aromatic}—O and C_{aliphatic}—O bonds. (62) On the other hand, Ru nanoparticles smaller than 4.0 nm exhibit higher activity in the hydrogenation of aromatic rings than larger nanoparticles. (63) In specific cases, even isolated Ru atoms have been found to be highly active in the hydrogenation of aromatic rings. (64) Our ongoing and future work is centered on enhancing the control of Ru speciation within the catalyst to address this complexity and better understand how different Ru species contribute to overall catalytic behaviour, enabling us to refine the design of the catalyst to achieve improved performance.

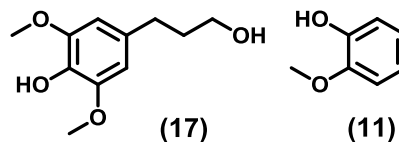
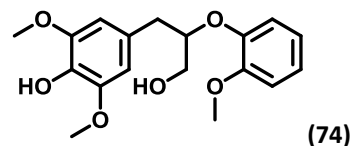
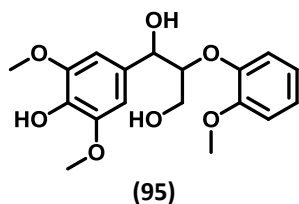
Final tests with a type C β-O-4 model and a lignin oil model mixture.

To take one step further and evaluate the potential of our Ni₇Co₃@Ru catalyst in the depolymerization of a real lignin, a more realistic model had to be chosen. Specifically, the β-O-4 linking motif is the most common structural unit in native lignin across different types of biomasses. In that sense, although 2-phenoxy-1-phenylethanol has the α-hydroxyl group present in the native β-O-4 motif, it lacks the γ-hydroxyl group, and the aromatic ring is unsubstituted, all of which may result in a significantly different reactivity. Consequently, we selected 1-(4-hydroxy-3,5-dimethoxyphenyl)-2-(2-methoxyphenoxy)propane-1,3-diol, a compound of the β-O-4 Type C family, which is considered to be the most representative set of compounds for the β-O-4 linking motif. (42) In Table 5, it can be seen that around 30% of C—O cleavage was attained after 60 h of reaction at 3H₂ bar under an AMF of 65 mT and a frequency of 300 kHz (see Table S6 for shorter reaction times). The main products obtained after this transformation were 4-(3-hydroxy-2-(2-methoxyphenoxy)propyl)-2,6-dimethoxyphenol, which corresponds to the loss of the —OH group in α, and the products which would be representative of the depolymerization yield (i.e., guaiacol, dihydrosynapyl alcohol, 4-propylsyringol). This degree of C—O cleavage suggests potential for lignin depolymerization. Nonetheless, improvements to the catalyst seem necessary to enhance the reaction rate for the C—O cleavage, such as optimizing Ru loading and speciation or adding supports to tune substrate adsorption.

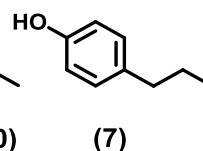
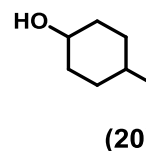
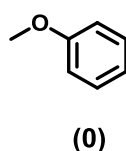
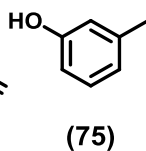
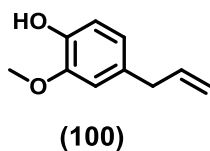
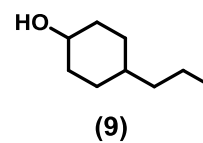
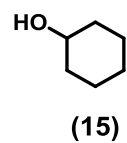
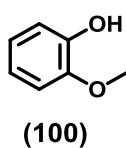
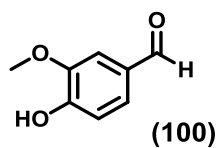
Table 5. Catalytic tests with Ni₇Co₃@Ru NPs in the hydrogenation of a C β-O-4 lignin linkage model and a lignin oil model mixture.

Reactant/s	Substrate Conversion	Yield of Main Products (mol.%, carbon basis)

β -O-4 Type C
lignin model^a



Lignin oil model
mixture^b



Reaction conditions: Batch-type reactor; a) 0.1 mmol substrate, 1.0 mL THF- d_6 , 1.5 mg $Ni_7Co_3@Ru$, AMF 300 kHz, 65 mT, 3 H_2 bar; b) 1.0 mmol substrates (0.20 mmol vanillin, 0.20 mmol anisole, 0.20 mmol guaiacol, 0.20 mmol eugenol, 0.20 mmol m-cresol) 0.25 mmol dodecane, 5 mL solvent (3 mL decane + 2 mL THF), 8 mg cat (≈ 0.1 metallic mmol), AMF 300 kHz, 65 mT, 3 H_2 bar.

Additionally, to assess the effectiveness of $Ni_7Co_3@Ru$ -NPs in lignin oil upgrading, a mixture containing anisole, guaiacol, vanillin, m-cresol and eugenol, which were molecules previously used, was prepared and subjected to a 60-hour long reaction (Table 5, entry 2). It was found that, from a relatively complex reaction mixture in terms of functionalities, we ended up having a mixture comprising mainly cyclohexanols, which, as for Ni_7Co_3 -NPs, indicates the good activity of the $Ni_7Co_3@Ru$ catalyst in aromatic ring hydrogenation and demethoxylation of ortho-substituted monomethoxyphenols. Another important observation is that, for the studied reaction time, the anisole remained unreacted. This is especially interesting considering that demethoxylation of anisole exhibited the highest reaction rate in the previous tests carried out with Ni_7Co_3 NPs using isolated substrates. In the same line of previous observations made while studying DPE and 4-phenoxyphenol, it is likely that the selective adsorption of $-OH$ groups on the catalyst surface prevents hydrophobic molecules from interacting with it. Similar to the pure Ni_7Co_3 system, this catalyst is not capable of performing more challenging reactions such as deoxygenation that involves removing $-OH$ from phenol or dehydrating cyclohexanol, most likely due to the absence of necessary oxygen adsorption sites and acidity. The presence of these sites could also assist in freeing up active sites on the surfaces of the metal nanoparticles.

CONCLUSIONS

In summary, we synthesized a family of NiCo-NPs using the organometallic approach from a previously unreported combination of metal precursors, i.e. $\text{Ni}[\text{PrNC}(\text{CH}_3)\text{N}^i\text{Pr}]_2$ and $\text{Co}[\text{N}(\text{SiMe}_3)_2]_2(\text{thf})$ complexes. The deep structural characterization of the herein-prepared nanoparticles by HR-EM, XAS and XRD suggests a complex interplay between the chemical elements composing them with a predominant fcc Ni-rich core, possibly doped with Co, and ultra-small (≤ 2 nm) hcp Co nanoparticles and clusters decorating it. Specifically, the Ni_7Co_3 composition exhibits impressive heating power and stability. This was demonstrated in the hydrogenolysis of diphenyl ether, which represents the first instance of NiCo nanoparticles approached through an organometallic method employed in magnetically induced catalysis in the liquid phase. Yet, the intricacies of cleaving C—O bonds in hydroxylated lignin linkage models pose a formidable challenge. Although the addition of ruthenium (Ru) could significantly enhance the catalytic efficiency, when using a more realistic β -O-4 Type C model, it becomes evident that further improvements are necessary to make the catalyst suitable for real lignin depolymerization. In that sense, understanding of the role of the different Ru species on the catalyst on the catalytic activity as well as the control of this speciation could result in a significant improvement in that direction. In addition, the Ni_7Co_3 and $\text{Ni}_7\text{Co}_3@\text{Ru}$ nanoparticles have shown promising behaviours in the upgrading of lignin oils through hydrodeoxygenation, with a significant preference for cyclohexanols. Nevertheless, there is still room for improvement in HDO due to the absence of distinct oxygen adsorption sites, such as oxygen vacancies, acid sites, or metal/oxide interfaces. Therefore, the introduction of support oxides is a tempting prospect for further enhancing the current system. It is worth noting that the system's performance was consistently assessed at very low H_2 pressures (3 bar), which proves the potential of magnetically induced catalysis as a promising tool in the mild hydroprocessing of lignin. This study paves the way for greener and more efficient technologies for converting lignin that could be coupled with intermittent energies.

ACKNOWLEDGEMENTS

The authors gratefully acknowledge the funding from the ERC Advance grant (MONACAT 2015-694159). The authors thank Alain Moreau (LCC, Toulouse) for the ICP analysis. G.M. and B.C. thank the European Union's Horizon 2020 research and innovation program under the FET-OPEN FLIX Grant Agreement No. 862179 for funding

REFERENCES

1. Pang, S. Advances in thermochemical conversion of woody biomass to energy, fuels and chemicals. *Biotechnol. Adv.* **2019**, *37* (4), 589–597. DOI: 10.1016/j.biotechadv.2018.11.004

2. Lange, J.-P. Towards circular carbo-chemicals—the metamorphosis of petrochemicals. *Energy Environ. Sci.* **2021**, *14* (8), 4358–4376. DOI: 10.1039/D1EE00532D
3. Rockström, J.; Gaffney, O.; Rogelj, J.; Meinshausen, M.; Nakicenovic, N.; Schellnhuber, H. J. A roadmap for rapid decarbonisation. *Science* **2017**, *355* (6331), 1269–1271. DOI: 10.1126/science.aah3443
4. Ganzer, C.; Mac Dowell, N. A comparative assessment framework for sustainable production of fuels and chemicals explicitly accounting for intermittency. *Sustain. Energy Fuels* **2020**, *4* (8), 3888–3903. DOI: 10.1039/C9SE01239G
5. Chen, C.; Yang, Z.; Hu, G. Signalling the cost of intermittency: What is the value of curtailed renewable power? *J. Clean. Prod.* **2021**, *302*, 126998. DOI: 10.1016/j.jclepro.2021.126998
6. Wang, W.E.I.; Tuci, G.; Duong-Viet, C.; Liu, Y.; Rossin, A.; Luconi, L.; Nhut, J.M.; Nguyen-Dinh, L.; Pham-Huu, C.; Giambastiani, G. Induction heating: An enabling technology for the heat management in catalytic processes. *ACS Catal.* **2019**, *9* (9), 7921–7935. DOI: 10.1021/acscatal.9b02471
7. Marbaix, J.; Mille N.; Carrey, J.; Soulantica, K.; Chaudret, B. Magnetically Induced Nanocatalysis for Intermittent Energy Storage: Review of the Current Status and Prospects. In *Nanoparticles in Catalysis: Advances in Synthesis and Applications*; Wiley, 2021, pp 307–329. DOI: 10.1002/9783527821761.ch14
8. Pérez-Camacho, M. N.; Abu-Dahrieh, J.; Rooney, D.; Sun, K. Biogas reforming using renewable wind energy and induction heating. *Catal. Today* **2015**, *242*, 129–138. DOI: 10.1016/j.cattod.2014.06.010
9. Díaz-Puerto Z. J.; Raya-Barón A.; van Leeuwen P. W. N. M.; Asensio J. M.; Chaudret B. Determination of the surface temperature of magnetically heated nanoparticles using a catalytic approach. *Nanoscale* **2021**, *13* (29), 12438–12442.
10. Asensio, J. M.; Miguel, A. B.; Fazzini, P.-F.; van Leeuwen, P. W. N. M.; Chaudret, B. Hydrodeoxygenation Using Magnetic Induction: High-Temperature Heterogeneous Catalysis in Solution. *Angew. Chem., Int. Ed.* **2019**, *58*, 11306–11310. DOI: 10.1002/anie.201904366
11. Marin, I. M.; De Masi, D.; Lacroix, L.-M.; Fazzini, P.-F.; van Leeuwen, P. W. N. M.; Asensio, J. M.; Chaudret, B. Hydrogenation and hydrogenolysis of biomass-based materials using FeNi catalysts and magnetic induction. *Green Chem.* **2021**, *23*, 2025–2036. DOI: 10.1039/D0GC03495A
12. Gyergyek, S.; Kocjan, A.; Grilc, M.; Likozar, B.; Hocevar, B.; Makovec, D. A hierarchical Ru-bearing alumina/magnetic iron-oxide composite for the magnetically heated hydrogenation of furfural. *Green Chem.* **2020**, *22* (18), 5978–5923. DOI: 10.1039/D0GC00966K
13. Gyergyek, S.; Grilc, M.; Likozar, B.; Makovec, D. Electro-hydrogenation of biomass-derived levulinic acid to γ -valerolactone via the magnetic heating of a Ru nanocatalyst. *Green Chem.* **2022**, *24* (7), 2788–2794. DOI: 10.1039/D2GC00102K
14. Huang, C.; Wang, Y.; Zhong, R.; Sun, Z.; Deng, Y.; Duan, L. Induction heating enables efficient heterogeneous catalytic reactions over superparamagnetic nanocatalysts. *Chin Chem Lett.* **2023**, *34* (9), 108101. DOI: 10.1016/j.cclet.2022.108101
15. Lin, S.H.; Hetaba, W.; Chaudret, B.; Leitner, W.; Bordet, A. Copper-Decorated Iron Carbide Nanoparticles Heated by Magnetic Induction as Adaptive Multifunctional Catalysts for the Selective Hydrodeoxygenation of Aldehydes *Adv. Energy Mater.* **2022**, *12* (42), 2201783.
16. Li, C.; Zhao, X.; Wang, A.; Huber, G. W.; Zhang, T. Catalytic Transformation of Lignin for the Production of Chemicals and Fuels. *Chem. Rev.* **2015**, *115*, 11559–11624. DOI: 10.1021/acs.chemrev.5b00155

17. Schutyser, W.; Renders, T.; Van den Bosch, S.; Koelewijn, S. F.; Beckham, G. T.; Sels, B. F. Chemicals from Lignin: an Interplay of Lignocellulose Fractionation, Depolymerisation, and Upgrading. *Chem. Soc. Rev.* **2018**, *47*, 852–908. DOI: 10.1039/c7cs00566k
18. Deuss, P. J.; Barta, K. From models to lignin: Transition metal catalysis for selective bond cleavage reactions. *Coord. Chem. Rev.* **2016**, *306*, 510-532. DOI: 10.1016/j.ccr.2015.02.004
19. Cheng, F.; Bayat, H.; Jena, U.; and Brewer, C.E. Impact of feedstock composition on pyrolysis of low-cost, protein-and lignin-rich biomass: A review. *J. Anal. Appl. Pyrolysis* **2020**, *147*, 104780. DOI: 10.1016/j.jaap.2020.104780
20. Leng, E.; Guo, Y.; Chen, J.; Liu, S.; Jiaqiang, E.; Xue, Y. A comprehensive review on lignin pyrolysis: Mechanism, modeling and the effects of inherent metals in biomass. *Fuel* **2022**, *309*, 122102. DOI: 10.1016/j.fuel.2021.122102
21. Garcia, A. C.; Cheng, S.; Cross, J. S. Solvolysis of Kraft Lignin to Bio-Oil: A Critical Review, *Clean Technol.* **2020**, *2* (4), 513-528. DOI: 10.3390/cleantechnol2040032.
22. Margellou, A.; Triantafyllidis, K.S. Catalytic transfer hydrogenolysis reactions for lignin valorization to fuels and chemicals. *Catalysts* **2019**, *9* (1), 43. DOI: 10.3390/catal9010043
23. Jing, Y.; Dong, L.; Guo, Y.; Liu, X.; Wang, Y.; Chemicals from lignin: a review of catalytic conversion involving hydrogen. *ChemSusChem* **2020**, *13* (17), 4181-4198. DOI: 10.1002/cssc.201903174
24. Agarwal, A.; Rana, M.; Park, J. H. Advancement in technologies for the depolymerization of lignin. *Fuel Process. Technol.* **2018**, *181*, 115-132. DOI: 10.1016/j.fuproc.2018.09.017
25. Bourbiaux, D.; Pu, J.; Rataboul, F.; Djakovitch, L.; Geantet, C.; Laurenti, D. Reductive or oxidative catalytic lignin depolymerization: An overview of recent advances. *Catal. Today* **2021**, *373*, 24-37. DOI: 10.1016/j.cattod.2021.03.027
26. Wang X.; Arai M.; Wu Q.; Zhang C.; Zhao F. Hydrodeoxygenation of lignin-derived phenolics – a review on the active sites of supported metal catalysts. *Green Chem.* **2020**, *22* (23), 8140-8168.
27. Shu, R.; Li, R.; Lin, B.; Wang, C.; Cheng, Z.; Chen, Y. A review on the catalytic hydrodeoxygenation of lignin-derived phenolic compounds and the conversion of raw lignin to hydrocarbon liquid fuels. *Biomass Bioenergy* **2020**, *132*, 105432. DOI: 10.1016/j.biombioe.2019.105432
28. Saidi, M.; Samimi, F.; Karimipourfard, D.; Nimmanwudipong, T.; Gates, B.C.; Rahimpour, M.R. Upgrading of lignin-derived bio-oils by catalytic hydrodeoxygenation. *Energy Environ. Sci.* **2014**, *7*, 103-129. DOI: 10.1039/C3EE43081B
29. Bruce D. W. *Transition Metal Sulphides: Chemistry and Catalysis*; Kluwer Academic Publishers, Dordrecht, 2000.
30. Alonso D. M.; Wettstein, S. G.; Dumesic J. A. Bimetallic catalysts for upgrading of biomass to fuels and chemicals. *Chem. Soc. Rev.* **2012**, *41* (24), 8075-8098. DOI: 10.1039/C2CS35188A
31. Cheng, C.; Shen, D.; Gu, S.; Luo, K.H. State-of-the-art catalytic hydrogenolysis of lignin for the production of aromatic chemicals. *Catal. Sci. Technol.* **2018**, *8* (24), 6275-6296. DOI: 10.1039/C8CY00845K
32. Shivhare, A.; Jampaiah, D.; Bhargava, S.K.; Lee, A.F.; Srivastava, R.; Wilson, K. Hydrogenolysis of lignin-derived aromatic ethers over heterogeneous catalysts. *ACS Sustainable Chem. Eng.* **2021**, *9* (9), 3379–3407. DOI: 10.1021/acssuschemeng.0c06715

33. Desvaux, C.; Amiens, C.; Fejes, P.; Renaud, P.; Respaud, M.; Lecante, P.; Snoeck, E.; Chaudret, B. Multimillimetre-large superlattices of air-stable iron–cobalt nanoparticles. *Nat. Mater.* **2005**, *4* (10), 750-753. DOI: 10.1038/nmat1480
34. Desvaux, C.; Dumestre, F.; Amiens, C.; Respaud, M.; Lecante, P.; Snoeck, E.; Fejes, P.; Renaud, P.; Chaudret, B. FeCo nanoparticles from an organometallic approach: synthesis, organisation and physical properties. *J. Mater. Chem.* **2009**, *19* (20), 3268-3275. DOI: 10.1039/B816509B
35. De Masi, D.; Asensio, J.M.; Fazzini, P.F.; Lacroix, L.M.; Chaudret, B. Engineering iron–nickel nanoparticles for magnetically induced CO₂ methanation in continuous flow. *Angew. Chem., Int. Ed.* **2020**, *59* (15), 6187-6191. DOI: 10.1002/anie.201913865
36. Tian, Z.; Liang, X.; Li, R.; Wang, C.; Liu, J.; Lei, L.; Shu, R.; Chen, Y. Hydrodeoxygenation of guaiacol as a model compound of pyrolysis lignin-oil over NiCo bimetallic catalyst: Reactivity and kinetic study. *Fuel* **2022**, *308*, 122034. DOI: 10.1016/j.fuel.2021.122034
37. Zhou, L.; Zhu, Z.; Luo, B.; He, Y.; Shu, R.; Tian, Z.; Wang, C. Bimetallic NiCo catalyzed enzymatic hydrolysis lignin hydrogenolysis to produce aromatic monomers. *Fuel* **2023**, *333*, 126357. DOI: 10.1016/j.fuel.2022.126357
38. Frederikse, H. P. R. *CRC Handbook of Chemistry and Physics*, D. R. LideCRC Press, Boca Raton, FL, 2009.
39. Ravel, B.; Newville, M. Athena, Artemis, Hephaestus: Data analysis for X-ray absorption spectroscopy using IFEFFIT. *J. Synchrotron Radiat.* **2005**, *12* (4) 537-541. DOI: 10.1107/S0909049505012719
40. Toby, B. H.; Von Dreele, R. B. GSAS-II: the genesis of a modern open-source all purpose crystallography software package. *Journal of Applied Crystallography* 2013, *46* (2), 544-549. DOI: 10.1107/S0021889813003531
41. Bordet, A.; Lacroix, L.-M.; Fazzini, P.-F.; Carrey, J.; Soulantica, K.; Chaudret, B. Magnetically Induced Continuous CO₂ Hydrogenation Using Composite Iron Carbide Nanoparticles of Exceptionally High Heating Power. *Angew. Chem. Int. Ed.* **2016**, *55*, 15894–15898. DOI: 10.1002/anie.201609477
42. Lahive, C.W.; Kamer, P.C.; Lancefield, C.S.; Deuss, P.J. An introduction to model compounds of lignin linking motifs; synthesis and selection considerations for reactivity studies. *ChemSusChem* 2020, *13* (17), 4238-4265. DOI: 10.1002/cssc.202000989
43. Almind M. R.; Vinum M. G.; Wismann S. T.; Hansen M. F.; Vendelbo S. B.; Engbæk J. S.; Mortensen P. M.; Chorkendorff I.; Frandsen C. Optimized CoNi nanoparticle composition for curie-temperature-controlled induction-heated catalysis *ACS Appl. Nano Mater.* **2021**, *4* (11), 11537–11544. DOI: 10.1021/acsanm.1c01941
44. Chaudret, B. Organometallic approach to nanoparticles synthesis and self-organization. *C. R. Phys.* **2005**, *6* (1), 117–131. DOI: 10.1016/j.crhy.2004.11.008
45. Palazzolo, A.; Poucin, C.; Freitas, A. P.; Ropp, A.; Bouillet, C.; Ersen, O.; Carencio, S. The delicate balance of phase speciation in bimetallic nickel cobalt nanoparticles. *Nanoscale* **2022**, *14* (20), 7547-7560. DOI: 10.1039/D2NR00917J
46. Oikawa, K.; Qin, G. W.; Ikeshoji, T.; Kainuma, R.; Ishida, K. Co (Cobalt) Binary Alloy Phase Diagrams. In *Alloy Phase Diagrams*, ASM, 2018, pp. 263-281. DOI: 10.31399/asm.hb.v03.a0006156

47. Zhao X. Q.; Veintemillas-Verdaguer S.; Bomati-Miguel O.; Morales M. P.; Xu H.B.; Thermal history dependence of the crystal structure of Co fine particles. *Phys. Rev. B* **2005**, *71* (2), 024106. DOI: 10.1103/PhysRevB.71.024106
48. Piotrowski, M. J.; Ungureanu, C. G.; Tereshchuk, P.; Batista, K. E.; Chaves, A. S.; Guedes-Sobrinho, D.; Da Silva, J. L. Theoretical Study of the Structural, Energetic, and Electronic Properties of 55-Atom Metal Nanoclusters: A DFT Investigation within van der Waals Corrections, Spin–Orbit Coupling, and PBE+U of 42 Metal Systems. *J. Phys. Chem. C* **2016**, *120* (50), 28844–28856. DOI: 10.1021/acs.jpcc.6b10404
49. Souto-Casares, J.; Sakurai, M.; Chelikowsky, J. R. Structural and Magnetic Properties of Large Cobalt Clusters. *Phys. Rev. B: Condens. Matter Mater. Phys.* **2016**, *93*, 1–6. DOI: 10.1103/PhysRevB.93.174418
50. Farkaš, B.; De Leeuw, N.H.; Towards a morphology of cobalt nanoparticles: size and strain effects. *Nanotechnology* **2020**, *31*(19), 195711. DOI: 10.1088/1361-6528/ab6fe0
51. Agostini, G.; Piovano, A.; Bertinetti, L.; Pellegrini, R.; Leofanti, G.; Groppo, E.; Lamberti, C.J.; Effect of different face centered cubic nanoparticle distributions on particle size and surface area determination: a theoretical study. *Phys. Chem. C*, 2014, *118* (8), 4085–4094. DOI: 10.1021/jp4091014
52. Mourdikoudis, S.; Collière, V.; Fau, P.; Kahn, M.L. A study on the synthesis of Ni₅₀Co₅₀ alloy nanostructures with tuned morphology through metal–organic chemical routes. *Dalton Trans.* **2014**, *43* (22), 8469-8479. DOI: 10.1039/C4DT00390J
53. Margeat O.; Amiens C.; Chaudret B.; Lecante P.; Benfield R.E. Chemical control of structural and magnetic properties of cobalt nanoparticles. *Chem. Mater.* **2005**, *17* (1), 107-11. DOI: 10.1021/cm048756a
54. de Julián Fernández, C.; Mattei, G.; Sangregorio, C.; Battaglin, C.; Gatteschi, D.; Mazzoldi, P. Superparamagnetism and coercivity in HCP-Co nanoparticles dispersed in silica matrix. *J. Magn. Magn. Mater.* **2004**, *272*, E1235-E1236. DOI: 10.1016/j.jmmm.2003.12.1111
55. Myrovali, E.; Papadopoulos, K.; Iglesias, I.; Spasova, M.; Farle, M.; Wiedwald, U.; Angelakeris, M. Long-Range Ordering Effects in Magnetic Nanoparticles. *ACS Appl. Mater. Interfaces* **2021**, *13*, 21602–21612. DOI: 10.1021/acsami.1c01820
56. Leal G.F.; Lima S.; Graça I.; Carrer H.; Barrett D.H.; Teixeira-Neto E., Curvelo A.A.; Rodella C.B.; Rinaldi R. Design of nickel supported on water-tolerant Nb₂O₅ catalysts for the hydrotreating of lignin streams obtained from lignin-first biorefining. *iScience* **2019**, *15*, 467–488. DOI: DOI: 10.1016/j.isci.2019.05.007
57. Cerny, C.; Ding, Y.-C.; Xiang, W.-J. Flavoring compositions. WO 2022/194879 A1, May 4, 2021.
58. Yang, Y.; Ochoa-Hernández, C.; Pizarro, P.; Coronado, J.M.; Serrano, D.P. Effect of metal–support interaction on the selective hydrodeoxygenation of anisole to aromatics over Ni-based catalysts. *Appl. Catal. B: Environ.* **2014**, *145*, 91-100. DOI: 10.1016/j.apcatb.2013.03.038
59. Yang, F.; Komarneni, M.R.; Libretto, N.J.; Li, L.; Zhou, W.; Miller, J.T.; Ge, Q.; Zhu, X.; Resasco, D.E. Elucidating the structure of bimetallic NiW/SiO₂ catalysts and its consequences on selective deoxygenation of m-cresol to toluene. *ACS Catal.* **2021**, *11*(5), 2935-2948. DOI: 10.1021/acscatal.0c05560
60. Schutyser, W.; Van den Bossche, G.; Raaffels, A.; Van den Bosch, S.; Koelewijn, S.F.; Renders, T.; Sels, B.F. Selective conversion of lignin-derivable 4-alkylguaiacols to 4-alkylcyclohexanols over noble and non-noble-metal catalysts. *ACS Sustain. Chem. Eng.* **2016**, *4* (10), 5336-5346. DOI: acssuschemeng.6b01580
61. Van den Bosch, S.; Schutyser, W.; Vanholme, R.; Driessen, T.; Koelewijn, S.F.; Renders, T.; De Meester, B.; Huijgen, W.J.J.; Dehaen, W.; Courtin, C.M.; Lagrain, B. Reductive lignocellulose fractionation into soluble

- lignin-derived phenolic monomers and dimers and processable carbohydrate pulps. *Energy Environ. Sci.* **2015**, *8* (6), 1748-1763. DOI: 10.1039/C5EE00204D
62. Dong, L.; Yin, L.L.; Xia, Q.; Liu, X.; Gong, X.Q.; Wang Y. Size-dependent catalytic performance of ruthenium nanoparticles in the hydrogenolysis of a β -O-4 lignin model compound. *Catal. Sci. Technol.* **2018**, *8* (3), 735-745. DOI: 10.1039/C7CY02014G
63. Zhao, H.; Song, H.; Zhao, J.; Yang, J.; Yan, L.; Chou, L. The reactivity and deactivation mechanism of Ru@C catalyst over hydrogenation of aromatics to cyclohexane derivatives. *ChemistrySelect* **2020**, *5*(14), 4316-27. DOI: 10.1002/slct.202000311.
64. Tang, N.; Cong, Y.; Shang, Q.; Wu, C.; Xu, G.; Wang X. Coordinatively unsaturated Al³⁺ sites anchored subnanometric ruthenium catalyst for hydrogenation of aromatics. *ACS Catal.* **2017**, *7*(9), 5987-91.